

A Survey of Small-Scale Waves and Wave-Like Phenomena in Jupiter's Atmosphere Detected by JunoCam

Glenn S. Orton¹, Fachreddin Tabataba-Vakili¹, Gerald Eichstädt², John Rogers³,
Candice J. Hansen⁴, Thomas W. Momary¹, Andrew P. Ingersoll⁵, Shawn Brueshaber⁶, Michael
H. Wong⁷, Amy A. Simon⁸, Leigh N. Fletcher⁹, Michael Ravine¹⁰, Michael Caplinger¹⁰, Dakota
Smith¹¹, Scott J. Bolton¹², Stephen M. Levin¹, James A. Sinclair¹, Chloe Thepenier¹³, Hamish
Nicholson¹⁴, Abigail Anthony¹⁵

¹Jet Propulsion Laboratory, California Institute of Technology, Pasadena, California, USA

²Independent scholar, Stuttgart, Germany

³British Astronomical Association, London, UK

⁴Planetary Science Institute, Tucson, Arizona, USA

⁵California Institute of Technology, Pasadena, California, USA

⁶Western Michigan University, Kalamazoo, Michigan, USA

⁷University of California, Berkeley, California, USA; SETI Institute, Mountain View, California, USA

⁸NASA Goddard Space Flight Center, Greenbelt, Maryland, USA

⁹University of Leicester, Leicester, UK

¹⁰Malin Space Science Systems, San Diego, California, USA

¹¹National Center for Atmospheric Research, Boulder, Colorado, USA

¹²Southwest Research Institute, San Antonio, Texas, USA

¹³Glendale Community College, Glendale, California, USA†

¹⁴Harvard College, Cambridge, Massachusetts, USA

¹⁵Golden West College, Huntington Beach, California, USA††

Corresponding author: Glenn Orton (glenn.orton@jpl.nasa.gov)

†currently at the University of California, Davis

††currently at the University of California, Berkeley

Key Points:

-In the first 20 orbits of the Juno mission, over 150 waves and wave-like features have been detected by the JunoCam public-outreach camera.

-A wide variety of wave morphologies were detected over a wide latitude range, but the great majority were found near Jupiter's equator.

-By analogy with previous studies of waves in Jupiter's atmosphere, most of the waves detected are likely to be inertia-gravity waves.

43 Abstract

44

45 In the first 20 orbits of the Juno spacecraft around Jupiter, we have identified a variety of wave-
46 like features in images made by its public-outreach camera, JunoCam. Because of Juno's
47 unprecedented and repeated proximity to Jupiter's cloud tops during its close approaches,
48 JunoCam has detected more wave structures than any previous surveys. Most of the waves appear
49 in long wave packets, oriented east-west and populated by narrow wave crests. Spacing between
50 crests were measured as small as ~30 km, shorter than any previously measured. Some waves are
51 associated with atmospheric features, but others are not ostensibly associated with any visible
52 cloud phenomena and thus may be generated by dynamical forcing below the visible cloud tops.
53 Some waves also appear to be converging and others appear to be overlapping, possibly at different
54 atmospheric levels. Another type of wave has a series of fronts that appear to be radiating outward
55 from the center of a cyclone. Most of these waves appear within 5° of latitude from the equator,
56 but we have detected waves covering planetocentric latitudes between 20°S and 45°N. The great
57 majority of the waves appear in regions associated with prograde motions of the mean zonal flow.
58 Juno was unable to measure the velocity of wave features to diagnose the wave types due to its
59 close and rapid flybys. However, both by our own upper limits on wave motions and by analogy
60 with previous measurements, we expect that the waves JunoCam detected near the equator are
61 inertia-gravity waves.

62

63 Plain Language Summary

64

65 The JunoCam camera aboard NASA's Juno mission to Jupiter has detected wave-like features over
66 its 20 orbits that are smaller and more numerous than ever seen before in Jupiter's atmosphere.
67 Most of the waves are in elongated wave packets, spread out in an east-west direction, with wave
68 crests that are often perpendicular to the packet orientation; others follow curved paths. The space
69 between wave crests can be as short as 30 kilometers. Some waves can appear close to other
70 atmospheric features in Jupiter, while others seem to have no relationship with anything nearby.
71 In one case, wave crests appear to be radiating outward from the center of a cyclone. Most waves
72 are expected to be atmospheric gravity waves - vertical ripples that form in the atmosphere above
73 something that disturbs air flow, such as a thunderstorm updraft, perturbations of flow around
74 other features, or from some disturbance from below that JunoCam does not detect. JunoCam is
75 uniquely qualified to make such discoveries, with its wide-angle field of view that delivers
76 sweeping vistas of the giant planet's atmosphere as the spacecraft swoops within about 2,100 miles
77 (3,400 kilometers) of Jupiter's cloud tops during each science pass.

78

79 Submitted to Journal of Geophysical Research - special issue on Juno results), 2019 December 31.

80

81 1. Introduction

82
83 The Juno mission’s JunoCam instrument (Hansen *et al.* 2017), conceived as a public-
84 outreach camera, has provided a surprising wealth of scientific results. These include the first
85 close-up examination of Jupiter’s polar regions (Orton *et al.* 2017), in particular the unexpected
86 presence and properties of constellations of cyclonic vortices around each pole (Adriani *et al.*
87 2018a, Tabataba-Vakili *et al.* 2019). JunoCam’s proximity to Jupiter’s cloud tops has also
88 provided high-resolution details of Jupiter’s Great Red Spot and its environment (Sánchez-Lavega
89 *et al.* 2018). These studies have been enabled by JunoCam’s wide field of view (58°) and the
90 close proximity of the spacecraft to the clouds being imaged, with target distances as small as
91 3,500 km near closest approaches (“perijoves”), yielding a horizontal pixel-to-pixel spacing as
92 good as 3 km.

93
94 We have used JunoCam’s coverage over a wide range of latitudes, coupled with its high
95 spatial resolving power, to examine all of our images for various phenomena in Jupiter’s clouds.
96 Small-scale waves, with wavelengths (distances between wave crests) less than ~300 km, were
97 first detected in 1979 by Voyager (Hunt and Muller, 1979) and have been detected by Galileo (e.g.
98 Bosak & Ingersoll, 2002) and New Horizons (e.g. Reuter *et al.*, 2007) since then, as well as by the
99 near-infrared JIRAM instrument on Juno (Adriani *et al.*, 2018; Fletcher *et al.* 2018). Larger waves,
100 with scales of 1200 km or greater, have since also been detected from the Earth using Hubble
101 Space Telescope (HST) and ground-based imaging (Simon *et al.*, 2018). A summary of
102 observations of these waves is given in Table 1, which includes and updates similar information
103 in Table 1 of Simon *et al.* (2015) and various tables in Simon *et al.* (2018). Table 1 includes a
104 JunoCam wave feature examined by Sánchez-Lavega *et al.* (2018) that we will also consider in
105 this report. No waves were detected by the Cassini mission, most likely because Cassini was too
106 far from Jupiter for adequate spatial resolution, but other reasons as possible. Virtually none were
107 seen by Galileo imaging despite several close, although spatially limited, passes. The planet-
108 encircling New Horizons waves were a surprise, as were the larger waves observed by HST and
109 ground-based imaging for the past four years, which Cassini would have detected. During the
110 Cassini epoch, there may not have been sufficient contrast to detect waves or waves were simply
111 not propagating because of conditions unknown.

112
113 Below, we describe how the measurements are made, followed by a survey of the different
114 types of atmospheric waves we have detected - along with any analogous wave formations in the
115 Earth’s atmosphere. We then discuss quantitative properties of the waves and conclude with an
116 analysis and discussion section.

119 2. Description of the measurements

120
121 JunoCam is a CCD-based camera, spanning a 58° field of view. The instrument is a “push-
122 frame” imager, taking advantage of Juno’s 2 RPM spin to sweep its 58° swath to build spatial and
123 spectral coverage without involving a shuttering mechanism. Thus, sequential images are acquired
124 in broadband blue, green and red filters plus a narrow-band filter centered on a 889-nm methane
125 absorption band. Time-delayed integration of multiple pixel rows builds up the signal-to-noise

126 ratio. Hansen *et al.* (2017) provide details of the instrument and its modes of operation. Sequential
127 images are typically rendered in red-green-blue (“RGB”) composites, with the “methane filter”
128 acquired and rendered separately, and the RGB images cover all latitudes on nearly all perijoves.
129 The spatial resolution varies with the distance to the planet, which changes with each orbit:
130 successive perijoves move approximately one degree of latitude north. For all the waves we
131 discuss in this report, the spatial resolution is much finer than the distances reported in each case.
132

133 In order to determine properties of the features, each image was transformed into a
134 cylindrical cartesian map in longitude and latitude. This was done independently of the standard
135 coordinate-transformation approach using the SPICE system (Acton 1996), as image timing,
136 orientation in the spacecraft coordinate system and optics distortion were still being determined.
137 We used limb fitting to constrain these properties, as the limb appears in all of our images. Current
138 SPICE data show good agreement with these maps, with the limb-fitting approach showing an
139 uncertainty better than 2° in the position of the south pole, as reported by Tabataba-Vakili *et al.*
140 (2019). Further details of this mapping process are provided by Adriani *et al.* (2018: see their
141 Supplementary Information) and by Tabataba-Vakili *et al.* (2019). All JunoCam images are
142 publicly available on the Mission Juno web site:

143 <https://www.missionjuno.swri.edu/junocam/processing>.

144
145 Figure 1 shows an example of a full JunoCam image, rendered in a cylindrically mapped
146 format, together with an excerpt (“crop”) of the image in which we identify wave-like features.
147 The mapped versions were adjusted to compensate for the variation of illumination across the field.
148 We found that a second-order power-law enhancement of color composites allowed wave features
149 to be identified more readily. For the images shown below, as well as in the Supplemental
150 Information, we further stretched each red, green and blue color independently for ease of
151 identification by the reader. We also applied unsharp-mask sharpening in a few cases to make
152 faint waves appear more prominently. Several coauthors independently searched manually through
153 all of the JunoCam images in order to identify wave-like features that were candidates for this
154 study. For detailed quantitative measurements, we used additional high-pass filtering to isolate
155 fine-scale features. Our quantitative measurements are based on maps of the images rendered with
156 180 pixels per degree of latitude and longitude, together with high-pass filtering. We did not find
157 identifiable wave features in any methane-band images. As a result, our discussion will be limited
158 to enhanced RGB-composite images. We did not see any consistent differences in the contrast of
159 wave features between the colors in images, which do not have any radiometric calibration.
160

161 3. Results

162 3.1 Overview.

163 We limited the search for and characterization of waves to observations between perijoves
164 1 and 20 (2016 August 27 – 2019 May 29). Hereafter we will abbreviate “perijove” as “PJ”.
165 During PJ2 (2016 October 19), no close-up images were made of Jupiter’s atmosphere as the result
166 of a spacecraft “safing” event immediately before close approach. During PJ19 (2019 April 6),
167 JunoCam only took distant images of Jupiter, as a result of an unusual orientation of the spacecraft
168 for most of that perijove in order to enable scanning in longitude by Juno’s Microwave Radiometer
169
170

171 (MWR) instrument. The Supplemental Information to this report documents and illustrates all of
172 the images in which we identified wave-like features with more than two wave fronts, together
173 with a visual aid to identify the waves. In this report we select particular images that provide
174 examples of the wide variety of waves and wave-like phenomena and their properties. The reader
175 is free to observe all the images that are available in various processed forms on the Mission Juno
176 web site in order to verify or refute our selections, as well as to identify potential additional
177 candidates.

178

179 3.2 Types of wave-like features.

180

181 Our survey of JunoCam images has revealed a surprising variety of features with wave-
182 like morphologies. In order to be inclusive in our inventory, we include here (and in the
183 Supplemental Information file) features with any regularly repeated patterns that are three or more
184 in number. The survey below includes many features that have not been discussed previously in
185 the context of atmospheric waves in Jupiter. They are presented in terms of differences in visual
186 morphology, without implication that this differentiation arises from the associated responsible
187 dynamics.

188

189 3.2.1 Long wave packets with short, dark wave fronts represent 79% of the types of waves
190 in our inventory, especially in the Equatorial Zone (EZ) that were also detected in previous studies,
191 particularly from Voyager imaging (Table 1).

192 3.2.1.1. Orthogonal wave crests. Figure 2 shows two examples of these waves in which the
193 wave front is more-or-less orthogonal to the direction of the wave packet. The morphology of the
194 waves shown in Fig. 2 is most similar to those waves described in the articles cited in Table 1,
195 although they are an order of magnitude smaller. They are most commonly referred to as mesoscale
196 waves, by analogy to their appearance in the Earth's atmosphere. Our search through JunoCam
197 images (see the images in the Supplemental Information file) did not appear to sample any of the
198 longer-wavelength (~1200-1900 km) packets detected by previous studies (Table 1), most likely
199 as a result of the limited area over which JunoCam images can cover.

200 3.2.1.2. "Tilted" wave crests. Even more commonly, the detected packets have wave
201 fronts that are not oriented orthogonally to the wavefront direction. Several examples of these
202 "tilted" wave fronts are shown in Figure 3. Simon et al. (2015) stated that this is consistent with
203 an interpretation of the waves as baroclinic instabilities that tilt northward and westward with
204 altitude, as noted on a theoretical basis by Holton (1992) and by observations of waves in the
205 Earth's atmosphere (e.g. Blackmon et al. 1984). This implies that we are sensing the upper
206 levels of such waves. Several images reveal the presence of large numbers of similar waves, as
207 shown in the various panels of Figure 4. The waves are most often short with wave packets
208 oriented east-west, although there are many wave packets not ostensibly oriented in any
209 preferred direction (Fig. 4D). Some clearly cross one another, implying that the sources of their
210 origin are not uniform. Simon et al. (2015b) argue that, if the waves are baroclinic instabilities,
211 then their meridional extent depends on the Rossby radius of deformation, which they estimate
212 as between 500 and 1400 km near the equator, which is where most of our detections of these
213 waves lie. The Rossby radius of deformation is also where energy is transferred from small-
214 scale turbulence to zonal winds (see Salyk et al. 2006, Young and Read 2017). Since the mean
215 of both meridional extent (~250 km on average) and wavelength (distance between wave crests,
216 ~170 km), are much shorter than the Rossby deformation radius, it is logical to assume that they

217 are formed by and interact with small-scale turbulence, and thereby propagate the waves in all
218 directions. This is consistent with our observation that few, if any, of these waves are clearly
219 associated with other atmospheric features.

220 3.2.1.3. Curved wave packets. Sometimes the short wavefronts are aligned in wave packets
221 that themselves appear to be curved, are associated with larger features, and are not located in the
222 EZ. Figure 5 shows two examples. Figure 5A shows the short wave-packets associated with the
223 curved northern boundary of the Great Red Spot (GRS) near 15.8°S, described by Sánchez-Lavega
224 et al. (2018). This is the first of two cases in which multiple images of waves were made, the result
225 of intensive targeting of the GRS by Juno at PJ7. Sánchez-Lavega et al. (2018) estimated a phase
226 speed for the wave of 45 ± 20 m/s relative to the very rapid local flow and determined that they
227 were consistent with internal gravity waves, given estimates for the Richardson number for that
228 part of the atmosphere that were based on the vertical wind shear deduced from temperature maps
229 of the region (Fletcher et al. 2010). Two other examples of such wave packets imaged at PJ15 are
230 shown. Figure 5B shows one on the south edge of a bright anticyclonic eddy in the NEB near
231 15.8°N, and Figure 5C shows one on the south edge of a dark cyclonic circulation in the SEB near
232 17.3°S. Just as for the wave trains in the northern edge of the GRS (Fig. 5A), these two wave
233 packets are located on or near the peaks of retrograde (westward) flows that are probably
234 accelerated in these locations because of the circulation.

235
236 Another curved wavefront example is shown in Figure 5D: a dark, lobate feature with short
237 wave crests that are most clearly detectable along its periphery. This feature is located in the
238 chaotic region to the west of the GRS (see Fig. 6 for context). Interestingly, the entire chaotic
239 region covers a much larger area to the northwest and west of the GRS, but these waves only
240 appear in the region shown in Figure 5D. The dark part of this lobate feature appears only slightly
241 brighter in 5- μ m radiance than its surroundings using contemporaneous NASA Infrared Telescope
242 Facility (IRTF) observations. Thus, it is likely to be a region of very moderate dry downwelling
243 that only partially clears out particles in cloud layers. Although the series of wave crests appears
244 to line the sharply curved periphery of the dark feature, the crests are more likely to be roughly
245 parallel streaks in a haze that overlies the entire region, with their visibility over the darker regions
246 of this image strongly subdued. This interpretation is reinforced by studies of the winds from
247 Juno-supporting observations by HST (Wong et al. 2020). Figure 6 shows the results of tracking
248 winds in this region. Relative to the mean zonal winds, the residual winds shown in this figure
249 appear to be flowing up toward the northwest along the dark lobe with speeds of 65 ± 17 m/s. Thus,
250 the waves appearing in Fig. 5D are aligned with the local retrograde flow in high-shear regions. In
251 this respect, they are similar to the curved wave packets described in the preceding paragraph.

252
253 3.2.2. Short wave packets with wide wave fronts, shown in Figures 7 and 8, are also
254 detected in our survey. In the Earth's atmosphere, such waves are often associated with
255 thunderstorms producing a brief impulse period with radiating waves. Other curved features
256 situated adjacent to each other are shown in the Supplemental Information file, which are shorter
257 and difficult to distinguish from different albedo clouds that are stretched along streamlines (see
258 Figs PJ05_108, PJ14_25a, PJ14_25b, and PJ14_25c.) Somewhat similar features were detected
259 in a Voyager image of "spiral" waves to the west of a dark brown cyclonic feature commonly
260 called a 'barge' (Simon et al. 2018). Although there is some overlap between these waves and
261 those described in section 3.2.1 in a spectrum of the length-to-width ratio of waves, these waves

262 appear to occupy a generally distinct locus in plot of the length vs width of waves (see Fig. SI3-2
263 in the Supplemental Information).

264
265 Other waves are even more distinct. The arrows in Figure 8 show extremely long, closely
266 spaced parallel lines that could be waves. Just as for the wave packets illustrated in Figure 7, both
267 are curved. The pair of lines indicated in the upper part of the figure appear to have no visual
268 association with any nearby feature, although they are situated between the bright (possibly
269 upwelling) spot to the north and the darker region to its south. This darker region is an extension
270 (sometimes called a “festoon”) of a blue-gray region along the southern boundary of the North
271 Equatorial Belt associated with bright 5- μm radiances, called a “5- μm hot spot”. The narrow dark
272 lines indicated in the bottom of Figure 8 are close to the southern boundary of the dark festoon.
273 Although they could simply be long streaks associated with streamlines of flow along the festoon,
274 they appear to be particularly narrow and well defined with sharp edges, particularly at their eastern
275 extents. This differentiates them particularly from far less distinct streaks along the northern
276 boundary of the festoon. They are also accompanied by shorter crests that are aligned
277 perpendicular to the length of the lines. These orthogonal waves are not explicitly indicated in
278 Figure 8 by white grids in order to make the extent of the long lines clearer, but they are illustrated
279 in the same region shown in the Supplemental Information file as Figure 20_34a. Orton et al.
280 (2017) detected linear features in the north polar region, but they were associated with the edge of
281 a well-defined haze region whose boundary could be traced using the 890-nm “methane” JunoCam
282 filter. JunoCam did not take images of the features indicated in Figure 8 with the 890-nm filter,
283 and they are below the spatial-resolution limits of Earth-based imaging in similar filters. The
284 closest morphological analogies in the Earth’s atmosphere might be roll clouds, formerly known
285 as cumulus cloud streets, e.g. Yang and Geerts (2014), which are most often detached from but
286 associated with a cumulonimbus base. These are now classified as volutus clouds
287 (<https://cloudatlas.wmo.int/clouds-species-volutus.html>) by the International Cloud Atlas.
288 Another possibility is that they represent a version of transverse cirrus clouds, identified in upper-
289 level tropospheric structures in the Earth’s atmosphere (Knox et al.2010).

290
291 3.2.3. Wave packets with bright features appear different from the waves indicated up to
292 this point (Figs. 2-7), which are recognizable by their dark or alternating dark-to-light crests.
293 JunoCam has imaged many waves and wave-like features that are manifested as regular, repeated
294 patterns of bright clouds, visually similar to terrestrial water-based clouds. We presume that
295 differences between darker and brighter wave crests could be the composition of the material
296 affected. Possibly the waves themselves induce condensation of bright white clouds along their
297 crests, similar to what was seen in the mid-NEB on much larger scales by Fletcher et al. (2017).
298 This might imply differences in altitude, e.g. perturbations of an upper-tropospheric haze layer
299 near 200-300 mbar (e.g. Sromovsky et al., 2017, and Braude et al. 2020) versus those of a
300 condensate cloud, such as a layer of “cirrus” NH_3 ice particles near the 600-mbar condensation
301 level. This corresponds to an altitude difference near the equator of roughly 15-20 km, an interval
302 on the order of or less than an atmospheric scale height.

303
304 Figure 9 shows a variety of examples of regular spacings between light-colored clouds
305 detected by JunoCam. We lack the means to determine whether dark regions adjacent to lighter
306 ones simply represent lower-albedo regions that are relatively cloudless or actual shadows of the
307 brighter clouds. One likely exception to this are the clouds associated with the wave packet in the

308 upper-left area of Figure 9A, which appear similar to terrestrial cirrocumulus clouds that have
309 shadows associated with them. (If all of the dark area to the right of the largest dark region is a
310 shadow, then the height of the largest cloud relative to the region around the cloud is on the order
311 of 10 km.) We repeat the caveat of Simon et al. (2015) that such dark features may not be shadows
312 but local regions of aerosol clearing “as atmosphere parcels rise and ices condense out to make the
313 wave crests”. The clouds in the other panels are often arranged in a straight line or a segmented
314 straight line with cirrus-like wisps trailing away from them. Figure 10 shows other regular patterns
315 of bright clouds that are associated with narrower white features. The narrow meridional extent of
316 these clouds (~150 km or less) is potentially the result of a very meridionally constrained flow.
317 We note that both are curved and could be associated with constraining wind flows.
318

319 Figure 11 shows four instances of very bright, discrete clouds forming regular, extended
320 patterns. These clouds extend to higher altitudes than their surroundings, as evidenced by shadows
321 that often accompany them. Individual clouds such as these appear in various locations elsewhere
322 in the planet, and we will describe and analyze them as a class in a separate report. We include
323 this subset of them in our description of a distinct type of wave. Figure 11A shows a close up of
324 such clouds, an expanded portion of Fig. PJ04_103b in the Supplemental Information file. A wave
325 packet can be seen that appears to be controlling small, bright cloud features. These are located in
326 a bright patch that is part of a complex system of upwelling disturbances in the North Equatorial
327 Belt (NEB), also known as ‘rifts’. Figure 11B shows a weak anticyclonic feature, in the center of
328 which is a central bright cloud, accompanied to its southeast through southwest by short linear
329 arrays of similar bright clouds. Two are shown with white grids that indicate individual cloud
330 features that are resolved. Figures 11C and 11D also show individual clouds that comprise a wave
331 packet, similar to the linear packet shown in Figure 11A. In Figure 11C, the clouds appear like
332 balls or small smears, whereas in Figure 11D they appear like C-shaped arcs. If the dark regions
333 accompanying the clouds in Figs. 11B, 11C and 11D are shadows, it would imply that they are
334 clouds whose tops are higher than the surrounding darker cloud deck. Based on the incident angle
335 of illumination, we estimate from the length of its shadow that the central cloud in Fig. 11B is only
336 3-4 km above the surrounding cloud deck. A similar estimate for the range of shadow lengths
337 associated with various bright clouds in Fig. 11C implies that they are 5-12 km above the
338 surrounding cloud deck. From the shadows associated with several C-shaped arcs in Fig. 11D, we
339 estimate that they rise as much as 6-13 km above the background cloud deck. There are other
340 similar features in both Figs. 11C and 11D, but they are not fully resolved. Although we cannot
341 determine with absolute certainty that these clouds extend down to the level of the surrounding
342 cloud deck, that is the impression one gets if the accompanying dark regions are interpreted as
343 shadows. If these bright clouds do extend vertically downward to the surrounding cloud deck,
344 then they appear less like linear versions of stratiform clouds on the Earth, than a series of
345 upwelling cumulus clouds in which the intervening spaces between them simply represent regions
346 of compensating subsidence.
347

348 3.2.4. Lee waves are stationary waves generated by the vertical deflection of winds over
349 an obstacle, such as a mountain, a thermal updraft or a vertical vortex. Unlike the Earth, there are
350 no mountains in Jupiter’s atmosphere, but there may indeed be the dynamical equivalent. If the
351 long streaks in Figure 12 that stretch diagonally (upper left to the lower right) in the figure are
352 tracking streamlines associated with local winds, and the winds are moving from the northwest to
353 the southeast (upper left to the lower right in the figure), then the lee wave is the three-wavefront

354 feature indicated by the white grid lines that is orthogonal to the flow. This requires that the local
355 winds are passing not only around the bright upwelling anticyclonic vortex in the upper left of the
356 frame, but also over it, consistent with very subtle streaks seen over the bright vortex. We note
357 that not only the three waves indicated but also the lines that appear to be tracing the wind flow
358 are elevated above the background cloud field, as marked by the shadows on their eastern sides.
359 The most prominent of the shadows is on the eastern side of the central wave, the length of which
360 implies that the peak of the wave is some 10 km about the background cloud deck. This is, in fact,
361 the only example of such a wave in our survey. One reason could be that other atmospheric
362 features are too high to permit flow over them, compared with the relatively young anticyclonic
363 vortex in Figure 12.

364
365 3.2.5. Waves associated with large vortices are shown in Figure 13. Figure 13A shows a
366 very compact cyclonic feature with a set of extended radial wavefronts in the North Equatorial
367 Belt. These resemble similar structures in terrestrial cyclonic hurricanes. The waves delineated
368 in Figure 13A show morphological similarities to “transverse cirrus bands” (hereafter ‘TCB’)
369 identified in upper-level tropospheric structures on Earth (Knox et al. 2010). TCB are defined by
370 the American Meteorology Society as “*Irregularly spaced bandlike cirrus clouds that form nearly*
371 *perpendicular to a jet stream axis. They are usually visible in the strongest portions of the*
372 *subtropical jet and can also be seen in tropical cyclone outflow regions.*” (American
373 Meteorological Society 1999). TCBs are also frequently observed in midlatitude mesoscale
374 convective systems (MCS) and in extra-tropical cyclones. Numerical studies (Trier et al. 2010,
375 Kim et al. 2014) have successfully replicated these cloud features and therefore have provided
376 insight to their formation. Currently, there is no consensus regarding the dynamics responsible for
377 TCB in all their observed forms (Knox et al. 2010). Multiple interacting factors that have been
378 implicated in the genesis of these features, including gravity waves, Kelvin-Helmholtz
379 instabilities, weak or negative moist static stabilities, and vertical wind shears (Dixon et al. 2000,
380 Trier et al. 2010, Knox et al. 2010).

381
382 There are some common characteristics that TCB share in the Earth’s atmosphere. First,
383 the bands frequently originate in a region of anticyclonic vorticity, positive divergence, and in
384 weak or negative static stability (Trier et al. 2010). Second, the majority of the bands appear in
385 regions of strong relative vorticity gradient, and often persist beyond the life of the originating
386 MCS (Lenz 2009). Third, the bands are often oriented along the vertical wind gradient, which
387 provides surprising evidence they share some dynamical characteristics with boundary-layer
388 horizontal convective roll vortices (Trier et al 2010, Kim et al. 2014), commonly observed on Earth
389 as cloud streets (Yang & Geerts 2006). Fourth, there is evidence that gravity waves propagating
390 below the cirrus cloud deck, the release of latent heat within the bands, and longwave cooling
391 above and longwave warming below the bands appears to favor the formation of TCB. In addition
392 to Figure 13A, the wave-like features shown in Figs. 2A, 3D, 4A, 5, 9A, and 9C appear similar to
393 terrestrial TBC. Although it is difficult to know if they are true analogs in the absence of detailed
394 horizontal wind measurements of these clouds (as well as temperature measurements to understand
395 the 3D wind gradients), their morphologies are suggestive. If this is the case, then complex small-
396 scale dynamics may be operating in and below the Jovian ammonia cloud deck not dissimilar to
397 those on Earth.

398

399 The wave features in Figure 13A bear some resemblance to similar features found in
400 tropical cyclones. Animations of tropical cyclones show high-frequency circular gravity waves in
401 the central dense overcast cirrus shield ('CDO', Molinari et al. 2014) emanating from vigorous
402 convection in or near the eyewall. Perhaps more relevant to the appearance of the features in Figure
403 13A, radial-aligned TCB are also commonly observed as 'spokes', which are more or less oriented
404 orthogonally to the gravity waves. In many cases, the circulation of the parent vortex twists the
405 spokes to appear like the teeth of a circular saw blade or as long thin curved filaments. In addition,
406 shallow-water numerical modeling of vortex dynamics using the Explicit Planetary Isentropic
407 Coordinate (EPIC; Dowling et al. 1998) in Brueshaber et al. (2019) also display curved wave-like
408 features similar to those in Figure 13A, but their waves are certainly due to gravity waves formed
409 during the merger of like-signed vortices for which we have no direct evidence in this figure.

410
411 On the other hand, for the much larger anticyclonic white oval in Figure 13B, it is possible
412 that the curved cloud features appearing there to be a manifestation of gravity waves. The spatial
413 resolution of this image is sufficient to see both the internal spiral structure of the white oval and
414 a regular set of dark bands extending to its exterior. Anticyclones on Jupiter, such this one, often
415 feature a high-speed 'collar' surrounding a calmer interior (e.g., Marcus 1993). The shear of the
416 high-speed wind against slower winds outside of the vortex may be sufficient to generate a Kelvin-
417 Helmholtz wave, which may explain the scalloped appearance of the white clouds adjacent to the
418 surrounding red clouds.

419
420
421 3.2.6. Long, parallel dark streaks are detectable at mid-latitudes. Long streaks are seen in many
422 areas of Jupiter's cloud system, usually with a non-uniform and chaotic pattern (e.g. the diagonal
423 ones in Fig. 12). But, as shown in Figure 14, some are seen in very regularly spaced parallel bands.
424 In several cases, the parallel banding is not only regularly spaced but sinusoidal in behavior, with
425 a distance between crests ranging between 280 and 360 km. All such features are detected far
426 from the equator. Their orientation suggests that they are tracing out the direction of flow on
427 streamlines, in often complicated patterns, with lengths from 500 km to 3800 km (an upper limit
428 that may be constrained by JunoCam's field of view). Almost all of the parallel streaks in the
429 examples shown in Fig. 14 are associated with larger atmospheric features, although those features
430 do not appear to be located where the streaks originate. In Figure 14A, one set of these appears to
431 be 'flowing' around an anticyclonic vortex in the lower left. It and a set of streaks in the center of
432 the feature have topography, with shadows apparent on their eastern sides. In Figure 14B, long
433 streaks possibly are associated with streamlines 'flowing' around small, red anticyclonic vortices.
434 The NTB was very turbulent at the time of these observations, following a great disturbance in the
435 preceding months (see Sánchez-Lavega et al. 2017). A semi-transparent triplet of short, dark bands
436 in the top left of this figure can be seen lying across longer bands that appear to be tracing wind
437 flow. Figure 14C shows parallel streaks located between a weak cyclonic eddy on the left and a
438 bright wave-like streak aligned with the SEBs retrograde jet, at the bottom edge of the panel.
439 Figure 14D shows several parallel cloud streaks in this turbulent part of the North North Temperate
440 Belt (NNTB). Some are associated with the small cyclonic vortex in the lower right side of the
441 panel. Often, the streaks appear to be on top of other features, implying that they represent flow
442 that is manifested in a haze layer overlying deeper cloud layers. The best analog to these features
443 lies not in the Earth's atmosphere but in Saturn's. Ingersoll et al. (2018) examine high-resolution
444 images of Saturn's clouds taken during the Cassini mission's "proximal orbits". Their Figure 3

445 shows a flow around a vortex that is very similar to one around the vortex in Figure 11A. For their
446 similar “thread-like filamentary clouds”, they suggest that the implied laminar flow implies
447 extremely low values of diffusivity and dissipation, which further quantitative analysis of these
448 observations may verify is the case for these scales in Jupiter, as well.

449
450 3.2.7. Unusual features are shown in Figure 15, which we might classify as waves only in the most
451 general sense. Figure 15A shows a series of features with a regular spacing: three curved
452 wavefronts next to an unusual series of relatively dark ovals indicated by the arrows. The dark
453 ovals may be connected dynamically to the wavefronts, because they continue in the same
454 direction and have roughly the same wavelength. The morphology of the three wave fronts implies
455 that flow is from the northwest. We do not see an array of short, dark, curved lines elsewhere, so
456 their spatial association with each other is extremely unusual. They are located near the boundary
457 between the turbulent northern component and the smooth, orange southern component of the
458 North Temperate Belt. Figure 15B shows a limited series of repeated patterns along the southern
459 edge of an unusual white band located at the turbulent boundary between the northern and southern
460 components of the North Temperate Zone. This short sequence bears some resemblance to a
461 Karman vortex street, although one that may be dissipating or disrupted.

462
463

464 3.3 Quantitative measurements of wave properties.

465
466

467 3.3.1. Measurements of meridional distribution and size properties.

468

469 Measurements were made of physical properties of all of the waves and wave-like features
470 discussed. A table of all of these is available in the Supplemental Information file. Features are
471 identified by Perijove and File number. Measured quantities are: the number of waves, the mean
472 System-III longitude, mean planetocentric latitude, length and width of the wave train, the mean
473 wavelength (distance between crests) and the tilt of the wave with respect to the orientation of the
474 wave packet.

475

476 Figure 16 shows a histogram of the occurrence of waves as a function of latitude. In order
477 for the reader to distinguish between different classes of wave-like features, some of which are
478 arguably not propagating waves, we have separated out the different types of waves by
479 morphology as discussed in the preceding sections. Table 2 shows our count of the different
480 categories of waves. The overwhelming majority of wave-like features are clustered between 7°S
481 and 6°N latitude, the relatively bright EZ. These features are dominated by long wave packets
482 with short wave crests, the type of waves detected by Hunt and Muller (1979) and discussed by
483 Simon et al. (2015a) as mesoscale waves observed at low latitudes by previous imaging
484 experiments. These waves fall within the relatively bright EZ and appear to be sub-clustered with
485 fewer waves between 1°S and the equator than between either 7°S and 1°S or the equator and 6°N.
486 The next most populous category are waves with short packet lengths and long crests, which appear
487 to be distinct not only because they appear to be clustered differently in length vs. width ratios, but
488 also because they mostly populate latitudes between 1°N and 3°N. Waves that are generally
489 associated with or influenced by larger features, most often associated with curved wave packets,
490 are the next most abundant feature. These include the curved wave packets at the northern

491 boundary of the GRS (Fig. 5A), the wave packets on the southern edge of a cyclonic circulation in
492 the SEB (Fig. 5b) and on the southern edge of an anticyclonic eddy (Fig. 5C), wave packets
493 associated with the lobate feature in the chaotic region west of the GRS (Fig. 5D), and parallel
494 stripes near a weak eddy (Fig. 14C). All are located in regions of retrograde flow, as shown in
495 Figure 17. All other types of features are detected less frequently (Table 2) and are scattered in
496 the northern hemisphere. No waves of any type were detected south of 7°S other than the ones
497 between 17°S and 20°S that are associated with larger features. There may be a small selection
498 effect associated with the observations, since latitudes in the northern hemisphere are observed
499 with an average spatial resolution that is higher than in the southern hemisphere, arising from the
500 fact that the Juno spacecraft perijove is in the northern hemisphere and moving northward by about
501 a degree of latitude for each successive, highly elliptical orbit. Perijove latitudes ranged from
502 3.8°N for PJ1 to 20.3°N for PJ20. Arguing against this is the fact that waves were detected in the
503 southern hemisphere with wavelengths between 70 km and 200 km, meaning that waves of this
504 size range would have been detectable elsewhere if they were present. Such waves might, in fact,
505 be present but undetectable if the hazes making them visible in the northern hemisphere were not
506 present in the southern hemisphere outside the EZ, for some reason.

507
508 Is the observed distribution of waves associated with other indicators of upwelling or
509 turbulence? Clearly the preponderance of waves in the EZ is not correlated with the frequency of
510 lightning detections, as no detections of lightning have been associated with that region, either
511 historically (e.g. Borucki & Magalhães 1992, Little et al. 1999, Dyudina et al. 2004) or in the broad
512 survey by the Juno Microwave Radiometer (Brown et al. 2018) that is sensitive to lightning
513 discharges in the EZ (Juno’s Waves instrument, Imai et al. [2018] could not detect lightning in the
514 EZ because the field lines do not reach Juno’s orbit.). The presence of water ice is one indirect
515 measure of upwelling, and its detection from Voyager IRIS data by Simon-Miller et al. (2000)
516 revealed a distribution that included the EZ but was significantly higher at latitudes south of ~10°S.
517 This is consistent with our results only in the limited sense that several waves were associated with
518 the GRS and its surroundings. Another indirect measure is the presence of pristine ammonia ice,
519 as measured most recently by New Horizons (Reuter et al. 2007), which determined that spectrally
520 identifiable ammonia clouds (SAICs) occurred “near active storms or upwelling regions”, which
521 includes some regions in the EZ and is more broadly consistent with several of our specific
522 observations at higher latitudes. New Horizons did not detect SAICs near the GRS, as the typically
523 chaotic region to its northwest was not active during the New Horizons encounter. From the Juno
524 mission itself, the striking deep column of concentrated ammonia at 2°N to 5°N detected by the
525 Microwave Radiometer (MWR) instrument implies upwelling (Li et al. 2017, Bolton et al. 2017),
526 which is consistent with the concentration of waves there. This is consistent with
527 contemporaneous ground-based observations (de Pater et al. 2019, Fletcher et al. 2016, 2020).
528 However, we detected an equal number of waves in the southern component of the EZ, where there
529 was not nearly as great a concentration of ammonia gas, so this particular correlation is imperfect.
530 We note that from studies of cloud properties from reflected sunlight, the full EZ is known as a
531 region in which tropospheric clouds and hazes extend higher than other locations on the planet
532 outside the GRS, as evidenced by the general concentration of upper-atmospheric opacity
533 historically (e.g. West et al. 1986) and in more recent work (see Figs. 4 and 12 of Sromovsky et
534 al. 2017, Fig 13B of Braude et al. 2020) or by the distribution of disequilibrium constituents (see
535 Fig. 4 of Orton et al. 2017b). This is consistent with the entire EZ being a region of general
536 upwelling.

537
538
539
540
541
542
543
544
545
546
547
548
549
550
551
552
553
554
555
556
557
558
559
560
561
562
563
564
565
566
567
568
569
570
571
572
573
574
575
576
577
578
579
580
581
582

Figure 17 plots the distribution of mean wavelengths for different types of waves and wave-like features as a function of latitude, co-plotted with mean zonal wind velocity. The minimum distance between crests is 29.1 km for the spacing between the discrete white features shown in Fig. 10A. Not significantly larger is the 30.9 km between crests of waves in a low-latitude long wave packet with short crests. These values are available in Table 1 of the Supplementary Information file. The variability of wavelengths within a single packet is typically no greater than 20-30%. The equatorial waves with long packets and short crests in the EZ have wavelengths that are clustered between 30 km and 320 km, with most between 80 and 230 km in size. The bimodal appearance of the distribution of EZ waves is not consistent with the distribution of waves detected from Voyager (Simon et al. 2015a), which also has several wave packets distributed at latitudes south of the EZ (see Figure 17). Similar to our study, most of these are associated with the GRS. Similar to Voyager, all the waves detected in JunoCam images in regions of retrograde flow are associated with discrete atmospheric features, such as the GRS. The virtual absence of waves observed in Voyager images covering the northern hemisphere is ostensibly the opposite of what we observe with JunoCam, although the key in Figure 16 shows that many of the wave-like features in the northern hemisphere might not have been categorized as waves by Voyager investigators.

3.3.2. Measurements of wave phase speed.

The most diagnostic criterion between different types of waves is the propagation speed. The waves in the EZ were discovered by Voyager 1 and described by Hunt & Muller (1979), who found them to have low or zero speeds relative to their surroundings (whether in a plume tail or equatorial clouds). Simon et al. (2015b) also found little relative motion for these waves in Voyager 2 and Galileo Orbiter images. Arregi et al.(2009), studying Galileo Orbiter images, likewise found no measurable relative motion for waves on the equator, but a phase velocity of 35 (+/-8) m/s for waves at 3°S. Simon et al. (2015b) adopted the conclusions of Flasar & Gierasch (1986), Bosak & Ingersoll (2002) and Arregi et al. (2009) that these waves detected by Voyager and Galileo images were best classified as inertia-gravity (IG) waves, a conclusion we do not revisit here. On the other hand, Simon et al. (2015b) differentiated the waves detected by New Horizons as Kelvin waves from those by Galileo and Voyager as IG waves on the basis of their phase velocity, crest length, and location; they measured a non-zero velocity (80±5 km/s) relative to the local zonal wind for the Kelvin waves that are confined to the equator compared with the IG waves, which are near stationary (upper limits to the phase velocity of 40 m/s or less). Unfortunately, the Juno spacecraft and orbit configuration that provides such close-up observations of Jupiter’s clouds strongly limits our ability to determine velocities, and regions are rarely observed at adequate spatial resolution more than once per perijove. Subsequent perijoves typically observe longitudes that are far from the preceding one. Observations of the Great Red Spot in PJ7 are one exception (Sánchez-Lavega et al. 2018), as noted above. Another is the circulation associated with a large cyclonic feature observed by both JunoCam and ground-based facilities (Iñurrigarro et al. 2020).

We made another attempt in PJ20 to observe one region several times during a perijove, focusing on the northern component of the EZ, Images 33 through 37 (formally JNCE_2019043_20C00033_V01 through JNCE_2019043_20C00037_V01). We examined these quite carefully using a recently developed upgrade in our geometric calibration, which used limb-

583 crossing times to correct for otherwise undetected errors in the data-acquisition timing. The results
584 showed no change in the location of waves (marked in Fig. PJ20_34a in the Supplemental
585 Information file near 27.5°W longitude and 0.5°N latitude) over the 6 min, 4-sec interval between
586 the first and last images of this sequence. We quantify this using a very conservative standard of
587 2 pixels for the pointing uncertainty, equivalent to 14 km for Image 33 and 18 km for Image 37 –
588 a linear dependence on the distance of the spacecraft from the waves. Using 16 km as an estimate
589 of the mean displacement, this is equivalent to an upper limit for the phase speed of 44 m/s, a value
590 consistent with a supposition that these are IG waves.

591
592 Moreover, based on morphology alone, the New Horizons waves were slightly curved, had
593 a consistent distance between wave fronts of 305 ± 25 km, a wave train that spanned the entire
594 visible equator (more than 200,000 km in packet length), and were centered at the equator,
595 spanning $\pm 2^\circ$ in latitude (see Figs. 1 and 2 of Simon et al. 2015). The waves that we detected here
596 have a broad range of wavelengths and crest lengths, are located at latitudes significantly far from
597 $\pm 1.5^\circ$ of the equator, and many wave packets are very short. Therefore, we suggest that these types
598 of waves detected in JunoCam images, more similar to those seen in Voyager and Galileo
599 observations, are most likely to be IG in origin.

600

601 4. Conclusions and future work

602

603 Juno’s public-outreach camera, JunoCam, detected a plethora of waves or wave-like
604 features in its first 20 perijove passes. Of these 157 features, 100 are waves with long, somewhat
605 linear packets and short crests are identified as mesoscale waves, consistent with earlier studies.
606 Many of these have wave crests that are nearly orthogonal to the wave packet orientation, although
607 others that were tilted compared with this orientation. Another 25 wave packets were detected
608 with short packets and long crests. As a group, they are likely to be features that are truly
609 propagating waves. They are more in number than was detected by Voyager imaging in 1979, and
610 they include waves that are smaller in wavelength than any detected by previous missions. These
611 waves form the vast majority of features detected in this study, and they are concentrated in a
612 latitude range between 5°S and 7°N. Short wave packets often appear in several different
613 orientations and sometimes overlap one another. Almost none of these appear to be associated
614 with other features except for waves that appear to be oriented in lines of local flow, including
615 packets with crests that appear darker than the local background or with bright features. These
616 bright features appear both as discrete, tall clouds with shadows that imply they are higher than
617 the background darker cloud deck, and simply as brighter features that have wispy “tails” and are
618 connected to one another by an equally bright but narrow, elongated cloud. The difference
619 between wide and narrow packets is presumably related to the width of the flow that is responsible
620 for the wave. There were fewer waves in the EZ between the equator and 1°N than there were
621 immediately north and south of this band, which was different from the waves detected by Voyager
622 imaging in 1979 that were more equally distributed.

623

624 Other waves, prominently those outside the EZ, are clearly associated with or influenced
625 by other features. These include short-crested packets following the slightly curved path at the
626 northern extent of the GRS, others associated with an anticyclonic eddy in the NEB and a cyclonic
627 circulation in the SEB, and one associated with the turbulent flow west of the GRS. Three lee
628 waves were detected in the wake of an upwelling anticyclonic vortex that were some 10 km above

629 the surrounding cloud deck. More features were detected that had repeated, wave-like features but
630 may not represent propagating waves. Some of the linear arrangements of discrete white clouds
631 followed the edges of vortices; although regular in spacing, these features may not represent
632 propagating waves so much as alternating positions of upwelling and subsiding vertical flows.
633 Several features appeared within or emanating from vortices. Two sets of extremely long, curved
634 features were detected near the edges of a southwestern extension of a dark blue-gray region
635 associated with high 5- μm radiances at the southern edge of the NEB. Long, sinuous parallel
636 streaks were detected, some with nearly sinusoidal lateral variability, that were analogous to
637 features observed by the highest-resolution imaging of Saturn's atmosphere by Cassini (Ingersoll
638 et al. 2018). No waves were detected south of 7°S that were not associated with larger vortices,
639 such as the GRS. No waves or wave-like features were detected in regions of retrograde mean
640 zonal flow that were not associated with larger features, similar to the waves detected by Voyager
641 imaging.

642
643 We had limited opportunities to classify waves on the basis of phase speed. Sánchez-
644 Lavega et al. (2018) determined that the waves located at the northern extent of the GRS were
645 internal gravity waves from their propagation speed with respect to the local flow, based on a
646 displacement over a 9-minute interval between initial and final images. (Internal gravity waves
647 are similar to IG waves but where Coriolis forces are not considered to be important.) JunoCam
648 seldom observes features more than once, and usually with insufficient time to note a
649 displacement. Our attempt to observe features in the EZ on PJ20 resulted in a 6-minute interval
650 over which no motions were detected for equatorial features, providing an upper limit of wave
651 motions that was not inconsistent with inertia-gravity waves. However, the waves detected in the
652 EZ were not located directly at the equator, which bounded the Kelvin waves detected by New
653 Horizons imaging (Simon et al. 2015b). Otherwise, the waves detected in the EZ are
654 morphologically similar to those detected by Voyager, which Simon et al. (2015b) classified as
655 inertia-gravity waves. These waves may well be associated generally with the upwelling winds
656 that characterize the EZ.

657
658 Work will continue to document and detect waves and wave-like features in Jupiter's
659 atmosphere, including further attempts to examine regions over longer time intervals, although we
660 note that observations of waves in the EZ will be lower in spatial resolution as the latitude of
661 successive perijoves migrates northward by about 1° per perijove. We will also look for
662 simultaneous measurements of waves in the near infrared by the JIRAM experiment to provide
663 some constraints on the altitude of these features, which were otherwise only loosely constrained
664 by occasional measurements of associated shadows. Furthermore, we expect that we and others
665 will use these observations as a motivation to engage in comparisons with terrestrial analogs and
666 numerical simulations that will further our understanding of the origin of these features and their
667 implications for the dynamics of Jupiter's atmosphere at these small scales and their relation to the
668 larger picture of planetary dynamics at depth.

669 5. Acknowledgements

670
671 Levin, Orton, Sinclair and Tabataba-Vakili were supported by funds from NASA distributed to
672 the Jet Propulsion Laboratory, California Institute of Technology. Bolton and Hansen were
673 supported by funds from NASA to the Southwest Research Institute and to the Planetary Science

674 Institute, respectively. Brueshaber was supported by Western Michigan University's Dissertation
675 Completion Fellowship. Ravine and Caplinger were supported by funds from NASA to Malin
676 Space Science Systems. Fletcher is a Juno Participating Scientist supported by a Royal Society
677 Research Fellowship and European Research Council Consolidator Grant (under the European
678 Union's Horizon 2020 research and innovation program, grant agreement No 723890) at the
679 University of Leicester. Wong was supported by NASA's Juno Participating Scientist program; a
680 part of his contribution was based on observations from program GO-14661, made with the
681 NASA/ESA Hubble Space Telescope, obtained at STScI, which is operated by AURA under
682 NASA contract NAS5-26555. Nicholson was supported by NASA funds to the Jet Propulsion
683 Laboratory as a participant in Caltech's Summer Undergraduate Research Fellowship (SURF)
684 program at JPL. Thepenier and Anthony were participants in JPL's Student Independent Research
685 Internship (SIRI) program.

686
687 All the images used in this study are available for direct download from the Mission Juno site:
688 <https://www.missionjuno.swri.edu/>

689
690 We note that preliminary results, including a version of Figure 11, were included in a NASA press
691 release: <https://www.jpl.nasa.gov/news/news.php?feature=7264>.

692
693 © 2019 All rights reserved.

694 References

- 695
696 Acton, C. H. 1996. Ancillary data services of NASA's navigation and ancillary information
697 facility. *Planet. Space Sci.* 44, 65-70.
- 698 Adriani, A., Mura, A., Orton, G., Hansen, C., Altieri, F., Moriconi, M. L., Rogers, J., Eichstädt,
699 G., Momary, T., Ingersoll, A., Filacchione, G., Sindoni, G., Tabataba-Vakili, F., Dinelli, B.
700 M., Fabiano, F., Bolton, S. J., Connerney, J. E. P., Atreya, S. K., Lunine, J. I., Tosi, F.,
701 Migliorini, A., Grassi, D., Piccioni, G., Noschese, R., Cicchetti, A., Plainaki, C., Olivieri, A.,
702 O'Neill, M. E., Turrini, D., Stefani, S., Sordini, R., Amoroso, M. (2018a) Clusters of cyclones
703 encircling Jupiter's poles. *Nature*. 555, 216-219. doi 10.1038/nature25491.
- 704 Adriani, A., Moriconi, M. L., Altieri, F., Sindoni, G., Ingersoll, A. P., Grassi, D., Mura, A.,
705 Atreya, S. K., Orton, G., Lunine, J. I., Fletcher, L. N., Simon, A. A., Melin, H., Tosi, Ciccetti,
706 A., Noschese, R., Sordini, R., Levin, S., Bolton, S., Plainaki, C., Olivieri, A. (2018b).
707 Characterization of mesoscale waves in the Jupiter NEB by Jupiter InfraRed Auroral Mapper
708 on board Juno. *Astron. J.* 156, 246 (12pp).
- 709 American Meteorological Society (1999). Glossary of Meteorology, 2nd edition, American
710 Meteorological Society: Boston, MA.
- 711 Allison, M. (1990). Planetary waves in Jupiter's equatorial atmosphere. *Icarus* 83, 282-307.
- 712 Arregi, J., Rojas, J. F., Hueso, R., Sanchez-Lavega, A. (2009) Gravity waves in Jupiter's
713 equatorial clouds observed by the Galileo orbiter. *Icarus* 202, 358-360.
- 714 Blackmon, M.L., Lee, Y.-H., & Wallace, J. A. (1984) Horizontal structure of 500 mb height
715 fluctuations with long, intermediate and short time scales. *J. Atmos. Sci.* 41, 961.
- 716 Bolton, S. J., Adriani, A., Adumitroaie, V., Anderson, J., Atreya, S., Boxham, J., Brown, S.,
717 Connerney, J. E. P., DeJong, E., Folkner, W., Gautier, D., Gulkis, S., Guillot, T., Hansen, C.,
718 Hubbard, W. B., Iess, L., Ingersoll, A., Janssen, M., Jorgensen, J., Kaspi, Y., Levin, S. M., Li,

719 C., Lunine, J., Miguel, Y., Orton, G., Owen, T., Ravine, M., Smith, E., Steffes, P., Stone, E.,
720 Stevenson, D., Thorne, R., Waite, J. (2017). Jupiter's interior and deep atmosphere: The first
721 close polar pass with the Juno spacecraft. *Science* **356**, 821-825.

722 Borucki, W. J., Magalhães, J. A. (1992) Analysis of Voyager 2 images of Jovian lightning.
723 *Icarus* **96**, 1-14.

724 Bosak, T. and Ingersoll, A. P. (2002). Shear instabilities as a probe of Jupiter's atmosphere.
725 *Icarus* **158**, 401-409.

726 Braude, A. S., Irwin, P. G. J., Orton, G. S., Fletcher, L. N. (2020). Colour and tropospheric cloud
727 structure of Jupiter from MUSE/VLT: Retrieving a Universal chromophore. *Icarus* In press.

728 Brown, S., Janssen, M., Adumitroaie, V., Atreya, S., Bolton, S., Gulkis, S., Ingersoll, A., Levin,
729 S., Li, Cl., Li, L., Lu nine, J., Misra, S., Orton, G. Steffes, P., Tabataba-Vakili, F., Kolmasova,
730 I., Imai, M., Santolik, O., Kurth, W., Hospodarsky, G., Gurnett, D., Connerney, J. (2018).
731 Prevalent lightning sferics at 600 megahertz near Jupiter's poles. *Nature* **558**, 87–90.
732 doi.org/10.1038/s41586-018-0156-5.

733 Brueshaber, S., Sayanagi, K., M., Dowling, T. E. (2019). Dynamical regions of giant planet polar
734 vortices. *Icarus* **323**, 46-61. doi 10.1016/j.icarus. 2019.02.001

735 de Pater, I., Sault, R. J., Moeckel, C., Moullet, A., Wong, M. H., Goullaud, C., DeBoer, D.,
736 Butler, B. J., Bjoraker, G., Adamkovics, M., Cosentino, R., Donnelly, P. T., Fletcher, L. N.,
737 Kasaba, Y., Orton, G. S., Rogers, J. H., Sinclair, J. A., Villard, E. (2019) First ALMA
738 millimeter-wavelength maps of Jupiter, with a multiwavelength study of convection.
739 *Astrophys. J.* **158**, 139 (17pp).

740 Dixon, R.S., Browning, K.A., Shutts, G.J. (2000). The mystery of striated cloud heads in satellite
741 imagery. *Atmospheric Science Letters*, doi:10.1006/asle.2000.0001

742 Dyudina, U. A., Del Genio, A. D., Ingersoll, A. O., Porco, C. C., West, R. A., Vasavada, A. R.,
743 Barbara, J. M. (2004). Lightning on Jupiter observed in the Ha line by the Cassini imaging
744 science subsystem. *Icarus* **172**, 24-36.

745 Flasar, F. M. and Gierasch, P. J. (1986). Mesoscale waves as a probe of Jupiter's deep
746 atmosphere. *J. Atmos. Sci.* **43**, 2683-2707.

747 Fletcher, L. N., Orton, G. S., Mousis, O., Yanamandra-Fisher, P., Parrish, P. D., Irwin, P. G. J.,
748 Edkins, E., Baines, K. H., Line, M. R., Vanzi, T., Fujiyoshi, T., Fuse, T. (2010). Jupiter's Great
749 Red Spot: High-resolution thermal imaging from 1995 to 2008. *Icarus* **208**, 306-328..

750 Fletcher, L. N. , Melin, H., Adriani, A., Simon, A. A., Sanchez-Lavega, A., Donnelly, P. T.,
751 Antuñaño, A., Orton, G. S., Hueso, R., Moriconi, M. L., Altieri, F., Sindoni, G. 2018. Jupiter's
752 mesoscale waves observed at 5 μ m by ground-based observations and Juno JIRAM. *Astron. J.*
753 **156**, 67 (13pp).

754 Fletcher, L. N., Greathouse, T. K., Orton, G. S., Sinclair, J. A., Giles, R. S., Irwin, P. G. J.,
755 Encrenaz, T. (2016) Mid-infrared mapping of Jupiter's temperatures, aerosol opacity and
756 chemical distributions with IRTF/TEXES. *Icarus* **278**, 128-161. doi
757 10.1016/j.icarus.2016.06.008

758 Fletcher, L. N., Orton, G. S., Greathouse, T. K., Zhang, Z., Oyafuso, F. A., Levin, S. J., Li, C.,
759 Bolton, S., Janssen, M., Mettig, H.-J., Rogers, J. H., Eichstädt, G., Hansen, C., Melin, H.,
760 Grassi, D., Mura, A., Adriani, A. (2020). Jupiter's equatorial plumes and hot spots: Spectral
761 mapping from Gemini/TEXES and Juno/MWR. *J. Geophys. Res.* (this issue).

762 Hansen, C., Caplinger, M. A., Ingersoll, Ravine, M. A., Jensen, E., Bolton, S., Orton, G. 2017.
763 Junocam: Juno's outreach camera. *Space Sci. Rev.* **217**, 475-506. doi:10.1007/s/11214-014-
764 0079-x.

765 Holton, J. R. 1992. An Introduction to Dynamic Meteorology (3rd ed.; New York; Academic
766 Press).

767 Hunt, G. E., and Muller, J.-P. (1979). Voyager observations of small-scale waves in the
768 equatorial region of the jovian atmosphere. *Nature* 280, 778-780.

769 Imai, M., Santolik, O., Brown, S., Kolmasova, IO., Kurth, W., Janssen, M., Hospodarsky, G.,
770 Gurnett, D., Bolton, S., Levin, S. (2018). Jupiter lightning-induced whistler and sferic events
771 with Waves and MWR during Juno perijoves. *Geophys. Res. Lett.* 45, 7268-7276.
772 doi.org/10.1029/2018GL078864.

773 Ingersoll, A. P., Ewald, S. P., Sayanagi, K. M., Blalock, J. J. (2018). Saturn's atmospheres at 1-10
774 kilometer resolution. *Geophys. Res. Lett.* 45, 7851-7856. doi.org/10.1029/2018GL079255.

775 Iñurrigarro, P., Hueso, R., Legarreta, J., Sánchez-Lavega, A., Eichstädt, G., Rogers, J. H., Orton,
776 G. S., Hansen, C. J., Pérez-Hoyos, S., Rojas, J. F., Gómez-Forrellad, J. M. 2020. Observations
777 and numerical modelling of a convective disturbance in a large-scale cyclone in Jupiter's South
778 Temperate Belt. *Icarus*. 336, 113475.

779 Kim, J-H., Chun, H-Y., Sharman, R.D., Trier, S.B. (2014). The role of vertical shear on aviation
780 turbulence within cirrus bands of a simulated western Pacific cyclone. *Monthly Weather*
781 *Review*, 142, 2794-2812.

782 Knox, J. A., Bachmeier, A. S., Carter, W. M., Tarantino, J. E., Paulik, L. C., Wilson, E. N.,
783 Bechdol, G. S., Mays, M. J. (2010). Transverse cirrus bands in weather systems: a grand tour
784 of an enduring enigma. *Weather* 65, 36-41.

785 Lenz, A., Bedka, K.M., Feltz, W.F., Ackerman, S.A. (2009). Convectively induced transverse
786 band signatures in satellite imagery. *Weather and Forecasting*, 24, 1362-1373.

787 Li, C., Ingersoll, A., Janssen, M., Levin, S., Bolton, S., Adumitroaie, V., Allison, M., Arballo,
788 A., Belotti, A., Brown, S., Ewald, S., Jewell, J., Misra, S., Orton, G., Oyafuso, F., Steffes, P.,
789 Williamson, R. (2017). The distribution of ammonia on Jupiter from a preliminary inversion of
790 Juno microwave radiometer data. *Geophys. Res. Lett.* 44, 5317-5325.

791 Li, L., Ingersoll, A. P., Vasavada, A. R., Simon-Miller, A. A., Achterberg, R. K., Ewald, S. P.,
792 Dyudina, U. A., Porco, C. C., West, R. A., Flasar, F. M. (2006). Waves in Jupiter's atmosphere
793 observed by the Cassini ISS and CIRS instruments. *s*, 416-429.

794 Little, B., Anger, C. D., Ingersoll, A. P., Vasavada, A. R., Senske, D. A., Breneman, H. H.,
795 Borucki, W. J., Galileo SSI Team (1999) Galileo images of lightning on Jupiter. *Icarus* 142,
796 306-323.

797 Marcus, P.S. (1993). Jupiter's Great Red Spot and Other Vortices. *Ann. Rev. Astron. Astrophys.*
798 31, 523-573.

799 Molinari, J., Duran, P., and Vollaro, D. (2014). Low Richardson number in the tropical cyclone
800 outflow layer. *Journal of the Atmospheric Sciences*. 71, 3164-3179.

801 Orton, G. S., Hansen, C., Caplinger, M., Ravine, M., Atreya, S., Ingersoll, A. P., Jensen, E.,
802 Momary, T., Lipkman, L., Krysak, D., Zimdar, R., Bolton, S. (2017a) The first close-up
803 images of Jupiter's polar regions: results from the Juno mission JunoCam instrument. *Geophys.*
804 *Res. Lett.* 44, 4599-4606. doi:10.1002/2016GL072443.

805 Orton, G. S., Momary, T., Ingersoll, A. P., Adriani, A., Hansen, C. J., Janssen, M., Arballo, J.,
806 Atreya, S. K., Bolton, S., Brown, S., Caplinger, M., Grassi, D., Li, C., Levin, S., Moriconi, M.
807 L., Mura, A., Sindoni, G. (2017b) Multiple-wavelength sensing of Jupiter during the Juno
808 mission's first perijove passage. *Geophys. Res. Lett.* 44, 4607-4614 doi:
809 10.1002/2017GL073019.

810 Porco, C. C., West, R. A., McEwen, A., Del Genio, A. D., Ingersoll, A. P., Thomas, P., Squyres,
811 S., Dones, L., Murray, C. D., Johnson, T. V., Burns, J. A., Brahic, A., Neukum, G., Veverka,
812 J., Barbara, J. M., Denk, T., Evans, M., Ferrier, J. J., Geissler, P., Helfenstein, P., Roatsch, T.,
813 Throop, H., Tiscareno, M., Vasavada, A. R. (2003). Cassini imaging of Jupiter's atmosphere,
814 satellites, and rings. *Science* 299, 1541-1547.

815 Reuter, D. C., Simon-Miller, A. A., Lunsford, A., Baines, K. H., Cheng, A. F., Jennings, D. E.,
816 Olkin, C. B., Spencer, J. R., Stern, S. A., Weaver, H. A., Young, L. A. (2007). Jupiter cloud
817 composition, stratification, convection, and wave motion: A view from New Horizons. *Science*
818 318, 223-225. doi 10.1126/science.1147618.

819 Rogers, J. (1995), *The Giant Planet Jupiter*, 418 pp., Cambridge Univ. Press, Cambridge, U. K.

820 Salyk, C., Ingersoll, A. P., Lorre, J., Vasavada, A., Del Genio, A. D. (2006) Interaction between
821 eddies and mean flow in Jupiter's atmosphere: Analysis of Cassini imaging data. *Icarus* 185,
822 430-442.

823 Sánchez-Lavega, A., Hueso, R., Eichstädt, G., Orton, G., Rogers, J., Hansen, C. J., Momary, T.,
824 Tabataba-Vakili, F., Bolton, S. (2018). The rich dynamics of Jupiter's Great Red Spot from
825 JunoCam – Juno images. *Astron. J.* 156, 162 (9 pp).

826 Simon-Miller, A. A., B. Conrath, P. J. Gierasch, R. F. Beebe. (2000). A detection of water ice on
827 Jupiter with Voyager IRIS. *I45*, 454-461.

828 Simon, A. A., Li, L., Reuter, D. C. (2015a). Small-scale waves on Jupiter: A reanalysis of New
829 Horizons, Voyager, and Galileo data. *Geophys. Res. Lett.* 42, 2612-2618, doi:
830 10.1002/2015GL063433.

831 Simon, A. A., Wong, M. H., Orton, G. s. (2015b). First results from the Hubble OPAL program:
832 Jupiter in 2015. *Astrophys. J.* 812:55 (8pp).

833 Simon, A. A., Hueso, R., Iñurrigarro, P., Sánchez-Lavega, A., Morales-Juberías, R., Cosentino,
834 R., Fletcher, L. N., Wong, M. H., Hsu, A. I. de Pater, I., Orton, G. S., Colas, F., Delcroix, M.,
835 Peach, D., Gómez-Forrellad, J.-M. (2018). A new, long-lived, jupiter mesoscale wave observed
836 at visible wavelengths. *Astron. J.*, 156:79 (18pp).

837 Sromovsky, L. A., Baines, K. H., Fry, P. M., Carlson, R. W. (2017) A possibly universal red
838 chromophore for modeling color variations on Jupiter. *Icarus* 291, 232-244. doi
839 10.1016/j.icarus.21016.12.014.

840 Sugiyama, K., Nakajima, K., Odaka, M., Kuramoto, K., Hayashi, Y.-Y. (2014). Numerical
841 simulations of Jupiter's moist convection layer: Structure and dynamics in statistically steady
842 states. *Icarus* 229, 71-91.

843 Sugiyama, K., Nakajima, K., Odaka, M., Kuramoto, K., Hayashi, Y.-Y. (2014). Corrigendum to:
844 "Numerical simulations of Jupiter's moist convection layer: Structure and dynamics in
845 statistically steady states. *Icarus* 229, 71-91]". *Icarus* 231, 407-408.

846 Tabataba-Vakili, F., Rogers, J. H., Eichstädt, G., Orton, G. S., Hansen, C. J., Momary, T. W.,
847 Sinclair, J. A., Giles, R. S., Caplinger, . A., Ravine, M. A., Bolton, S. J. (2019). Long-term
848 tracking of circumpolar cyclones on Jupiter from polar observations with JunoCam. *Icarus*. In
849 press.

850 Trier, S.B., Sharman, R.D., Fovell, R.G., Frehlich, R.G. (2010). Numerical simulation of radial
851 cloud bands within the upper-level outflow of an observed mesoscale convective system.
852 *Journal of the Atmospheric Sciences.* 67, 2990-2990.

853 West, R.A., Strobel, D. F., Tomasko, M. G. (1986). Clouds, aerosols, and photochemistry in the
854 Jovian atmosphere. *Icarus* 65, 161-217. doi 10.1016/0019-1035(86)90135-1

855 Wong, M. H., Simon, A. A., Tollefson, J. W., de pater, I., Barnett M., Hsu, A. I. Stephens, A.,
856 Orton, S. G. Fleming, S. W., Januszewski, W., Roman, A., Goullaud, C., Bjoraker, G. L,
857 Atreya, S. K., Adriani, A. (2020). High-resolution UV/optical/IR imaging of Jupiter in 2016–
858 2019. *Astrophysical Journal Supplement Series*. Submitted.

859 Yang, Q. and Geerts, B. (2014). Horizontal convective rolls in cold air over water:
860 Characteristics of coherent plumes detected by an airborne radar. *Monthly Weather Rev.* 134,
861 2373-2395.

862 Young, R. M. B., Read, P. L. (2017). Forward and inverse kinetic energy cascades in Jupiter’s
863 turbulent weather layer. *Nature Physics* 13, 1135.

864

865

866
867

Tables

Observing Platform (year)	Associated Publications	Range of Planetocentric Latitudes	Range of Wavelengths (km)
Voyager (1979)	Hunt & Muller (1979), Flasar & Gierasch (1986)	27°S-27°N	70-430
Galileo (1996)	Bosak & Ingersoll (2002)	13°S	300
Galileo (1999)	Arregi et al. (2009), Simon et al. (2015)	0.2°N, 3.6°N	155-205
Galileo (2001)	Arregi et al. (2009)	1.8°S	195-215
New Horizons (2007)	Reuter et al. (2007), Simon et al. (2015)	0°-1.1°N	280-330
Juno/JIRAM (2017)	Adriani et al. (2018), Fletcher et al. (2018)	14°-15°N	1400-1900
Juno/JunoCam (2017)	Sánchez-Lavega et al. (2018)	16°S	35
Hubble Space Telescope (2012-2018)	Simon et al. (2018)	14.5° ±2.5°N	1220-1340
Ground-Based Visible Observations (2017)	Simon et al. (2018)	14.5° ±2.5°N	1220-1340
Ground-Based 5-μm Observations (2016-2017)	Fletcher et al. (2018)	14.5° ±2.5°N	1300-1600

868
869
870
871
872
873
874
875
876
877
878
879
880
881
882

Table 1. Summary of previous observations of small-scale waves in Jupiter's clouds detected at 5 μm or shorter wavelengths. (Some values are also displayed in Figure 16.) The waves addressed by Sánchez-Lavega et al. (2018) are associated with the Great Red Spot.

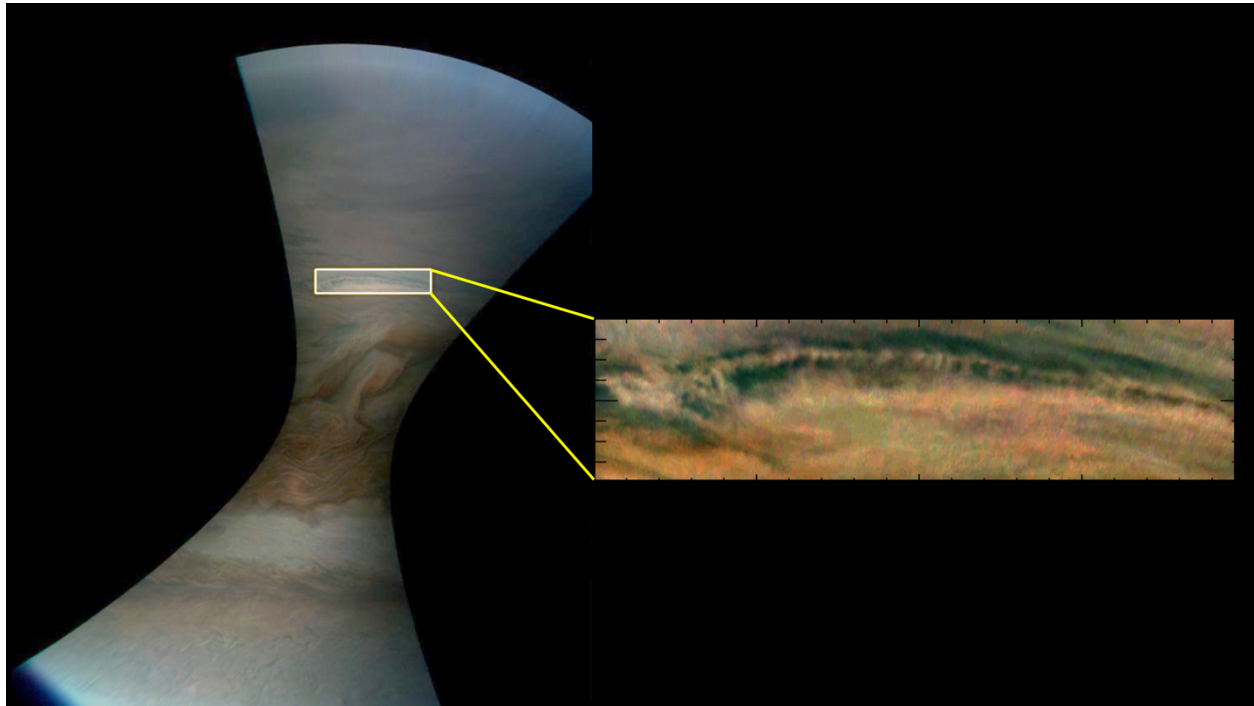
Type of Wave-Like Feature (section where discussed)	Number of Features
Long packets, short crests (3.2.1)	100
Wide wave crests (3.2.2)	25
Curved packets (3.2.1)	9
Small white clouds (3.2.3)	9
Regularly spaced dark features (3.2.7)	6
Emanating from vortex (3.2.5)	4
Extremely long curved features (3.2.2)	2
Lee waves (3.2.4)	1

883
884
885
886
887
888
889
890
891

Table 2. Number of features in each morphological category, listed in order of frequency. These include features not illustrated in the figures associated with the main article but included in the Supplementary Information file. The total number of waves or wave-like features is 157. The category of waves with long packets and short crests dominates the total. Quantitative properties of these waves are shown in the Table of Section SI2 of the Supplemental Information file. They are also shown graphically in Figs. 16, 17 and Figs. SI3-1 through SI3-3 of the Supplemental Information file.

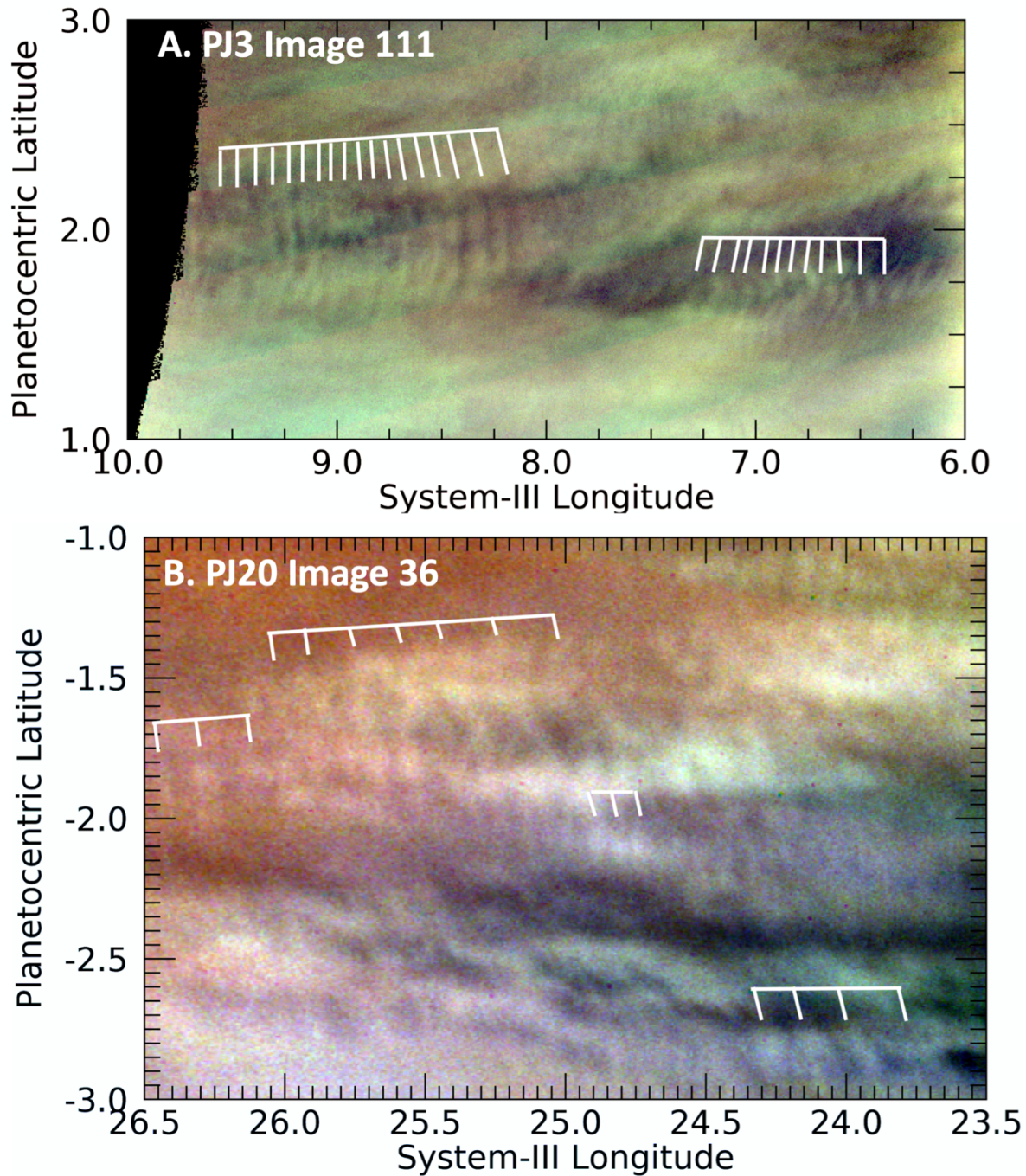
892
893

Figures



894
895
896
897
898
899
900
901

Figure 1. Example of excerpting a portion of a wave-like feature from a JunoCam image from planetocentric latitudes 3°S - 4°S. This is a cylindrical mapping of a color-composited Image JNCE_2017297_09C00088_V01 (which here and elsewhere we simply identify as Image 99 from PJ9). The extracted panel is also shown as Figure 10B and in the Supplemental Information file as Figure PJ09_88 with a grid indicating the location of peak radiances in the wave-like feature.



903

904

905 *Figure 2. Excerpts from JunoCam color-composite maps of images in PJ3 illustrating isolated*
 906 *wave packets with shorter wave fronts that are orthogonal to the orientation of the wave packet.*
 907 *In this and all other similar figures in this report, the colors have been stretched extensively in*
 908 *order to make the waves as visible as possible; they have absolutely no relationship with the true*
 909 *colors of the planet. In this and some sequent images here and in the Supplemental Information*
 910 *file, broad vertical or diagonal colored bands are artefacts of strong image enhancement to*
 911 *distinguish otherwise faint features.*

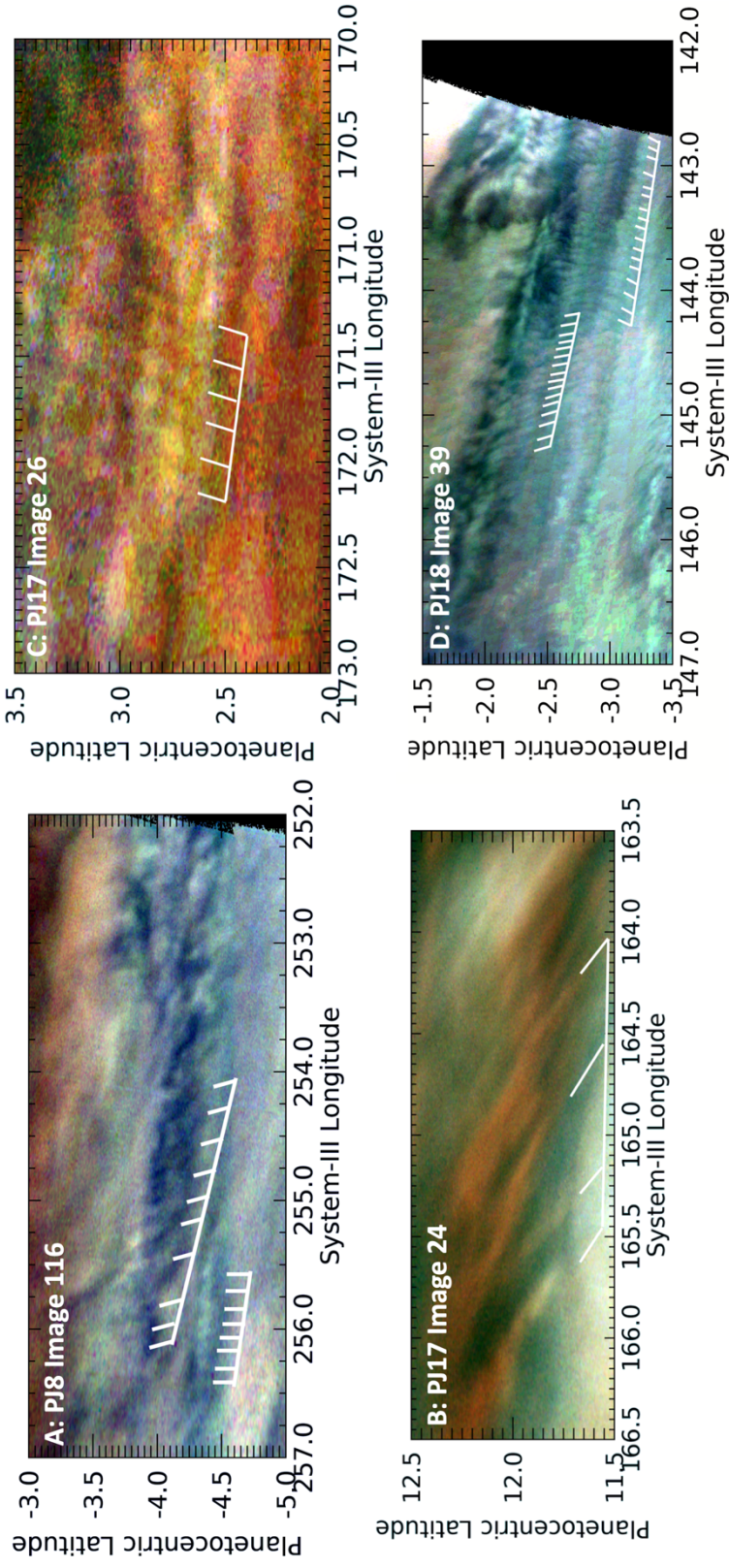


Figure 3. Excerpts from JunoCam maps of images in PJ8 (Panel A), PJ17 (Panels B and C) and PJ18 (Panel D). These illustrate individual wave packets with shorter wave fronts that are not-orthogonal (i.e. they are tilted) with respect to the orientation of the wave packet direction.

916
917
918
919

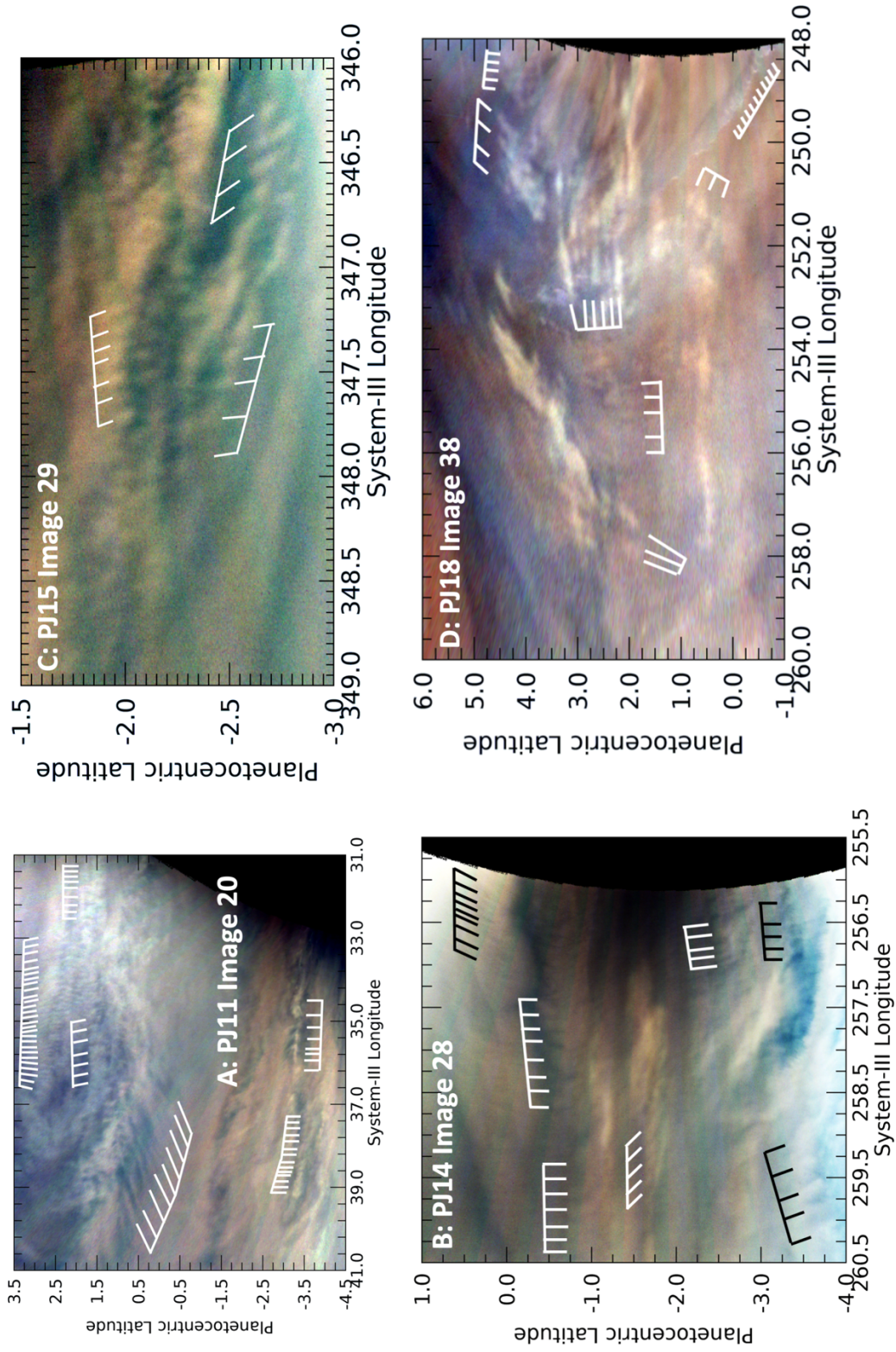


Figure 4. A variety of wave morphologies detected near the equator. As shown in these images, the Equatorial Region is often populated with both short and long wave trains with both orthogonal and tilted wave fronts, often overlapping. Toward the bottom of Panels A and D are a set of waves defined by discrete white clouds, more of which are shown closer up in Figure 8.

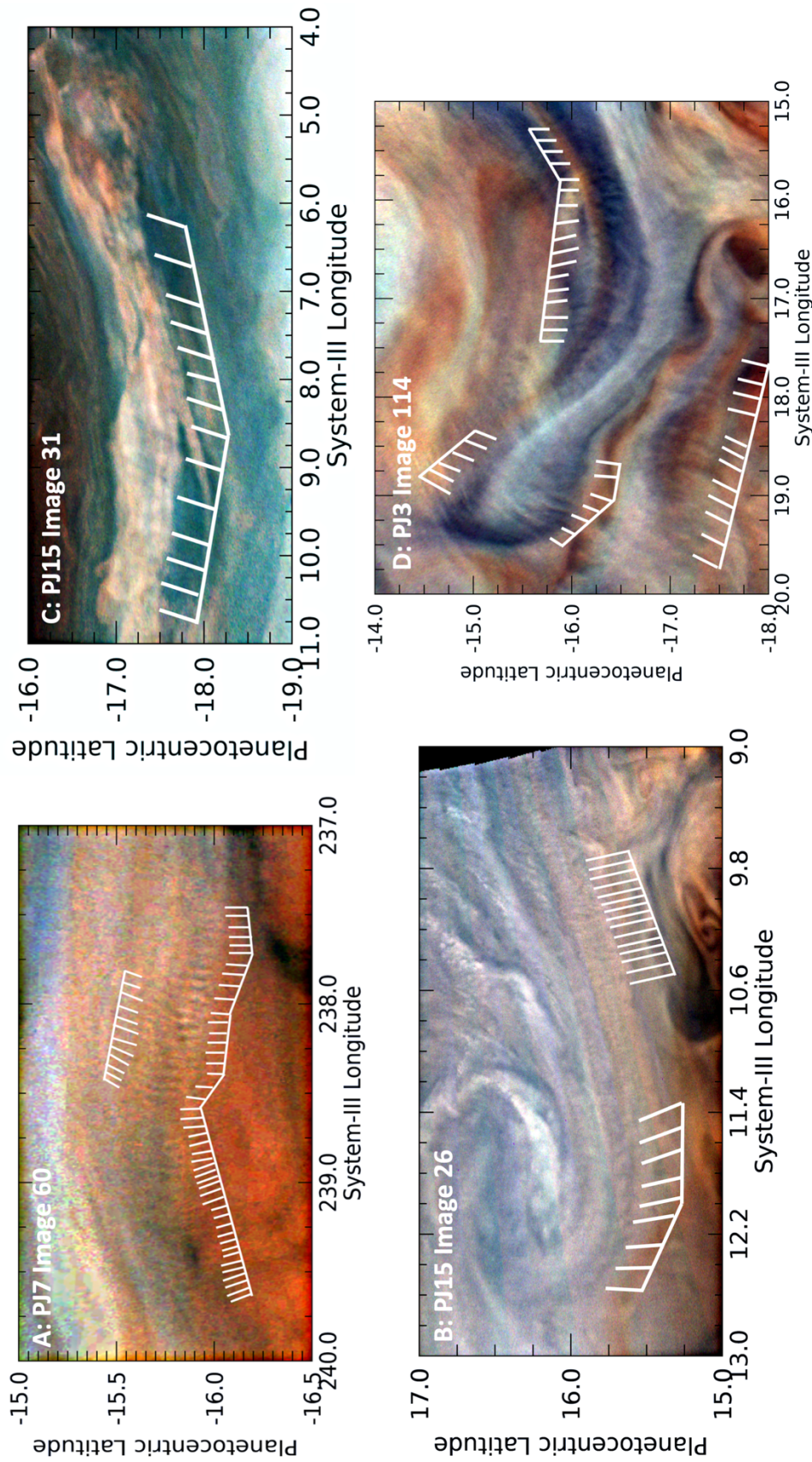
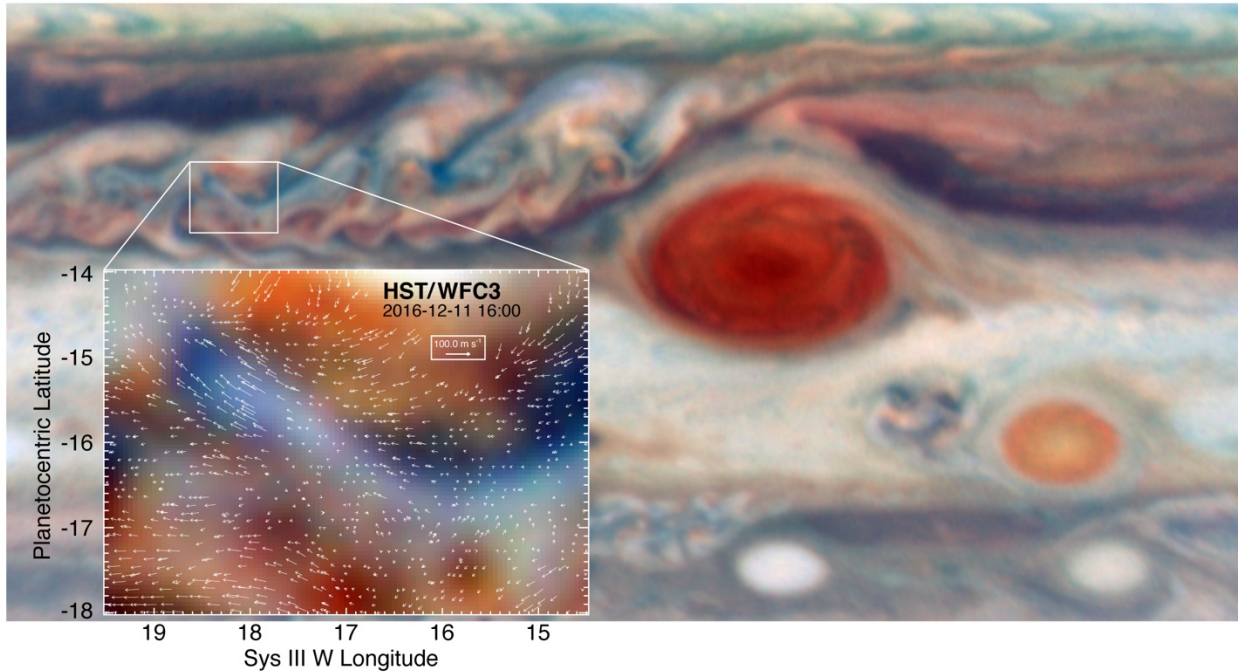
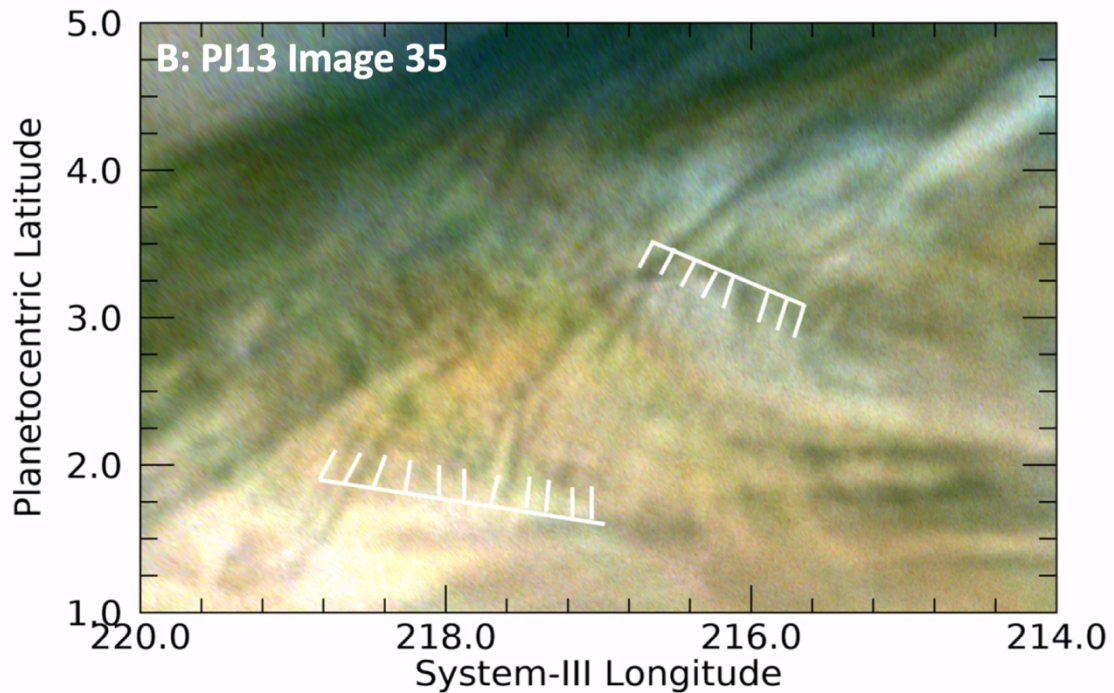
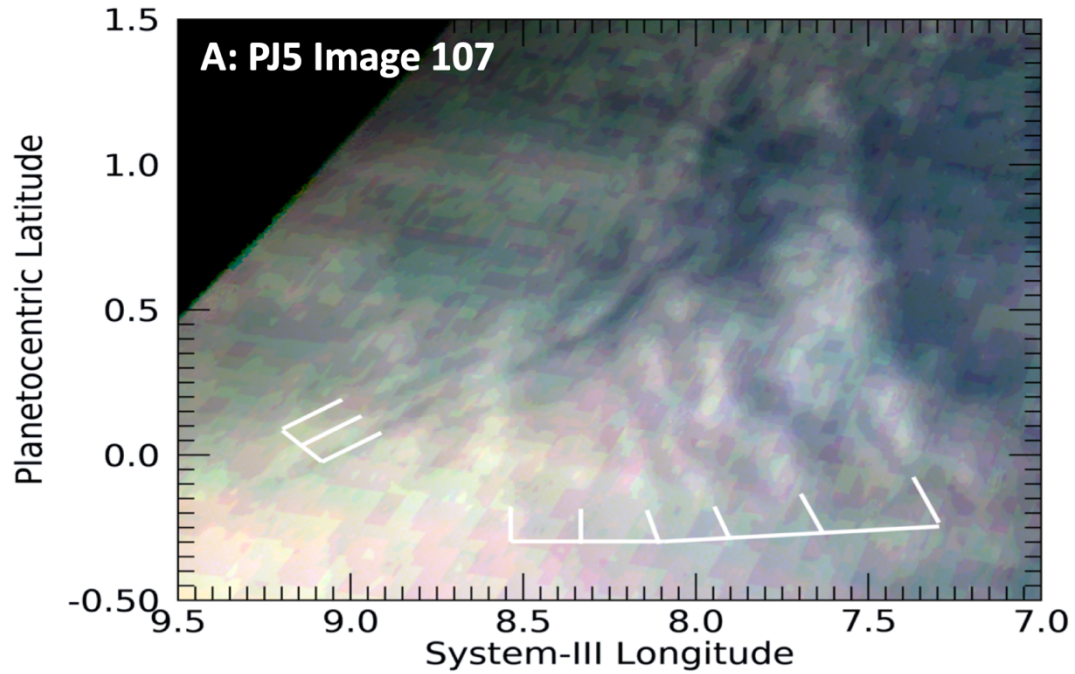


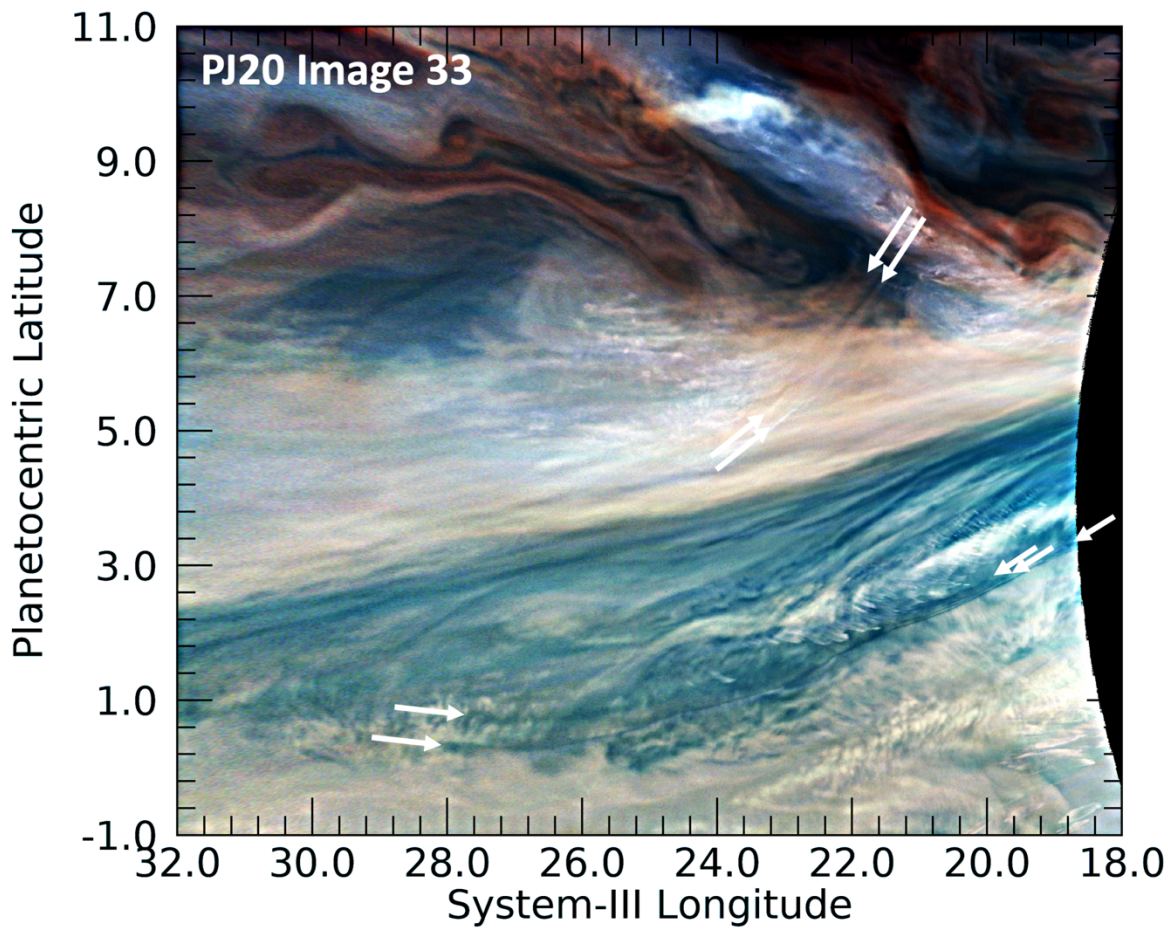
Figure 5. Examples of short wavefronts associated with a curved wave packet. A: Wavefronts associated with the curvature of the northern boundary of the GRS. A version of this panel appears in Figure 8 of Sánchez-Lavega et al. (2018). B: Wavefronts along the southern edge of an anticyclonic eddy in the NEB. C: Wavefronts on the south edge of a cyclonic circulation in the SEB. D: Wavefronts that cross a relatively dark lobate feature in the South Equatorial Belt (SEB), a part of a turbulent region west of the Great Red Spot.



921
 922 *Figure 6. Contextual HST WFC3 image for Figure 5D, showing its position with respect to the*
 923 *GRS. The inset shows the wind field derived from tracking cloud features over a 45-minute*
 924 *interval, as a residual after subtracting the mean zonal wind profile. The winds appear to be a*
 925 *maximum at the western (left) end of the blue lobate feature, with a marked drop in velocities, i.e.*
 926 *a region of wind shear, at the edges of the feature. This image was taken within a few minutes of*
 927 *the time at which the JunoCam image in Fig. 5D was observed*
 928



929
 930 *Figure 7. Excerpts from maps showing waves whose wave fronts are larger than the wave packet*
 931 *length. Both are curved and located in the Equatorial Zone. Panel A shows a pair of wave packets,*
 932 *overlapping each other, the westernmost of which contains at least three wave fronts that are much*
 933 *longer than the packet. The overlapping easternmost wave packet has wave fronts and a length*
 934 *that are roughly equal in size. Panel B shows a series of curved waves that appear to extend past*
 935 *the boundaries of the full image*



936
 937 *Figure 8. Extremely long, curved features detected in PJ20. Two unusually long features that may*
 938 *be waves were detected near the southwestern extension (“festoon”) of a 5- μ m hot spot, seen here*
 939 *as the dark area. North of the dark area of the festoon is a pair of lines, whose beginnings and*
 940 *ends are marked by white arrows. Among the many waves found south of the festoon, is a set of*
 941 *three closely spaced parallel lines, noted by the arrows that do not begin or end at the same*
 942 *position. Only for two of them is the western end evident. We note that some mild unsharp masking*
 943 *has been applied to this image in order to resolve for the reader the three dark curves at their*
 944 *eastern ends. (The locations of many more of the waves present in this figure are indicated in*
 945 *Figure PJ20_34 in the Supplemental Information file.)*

946
 947
 948
 949

950
 951
 952
 953
 954

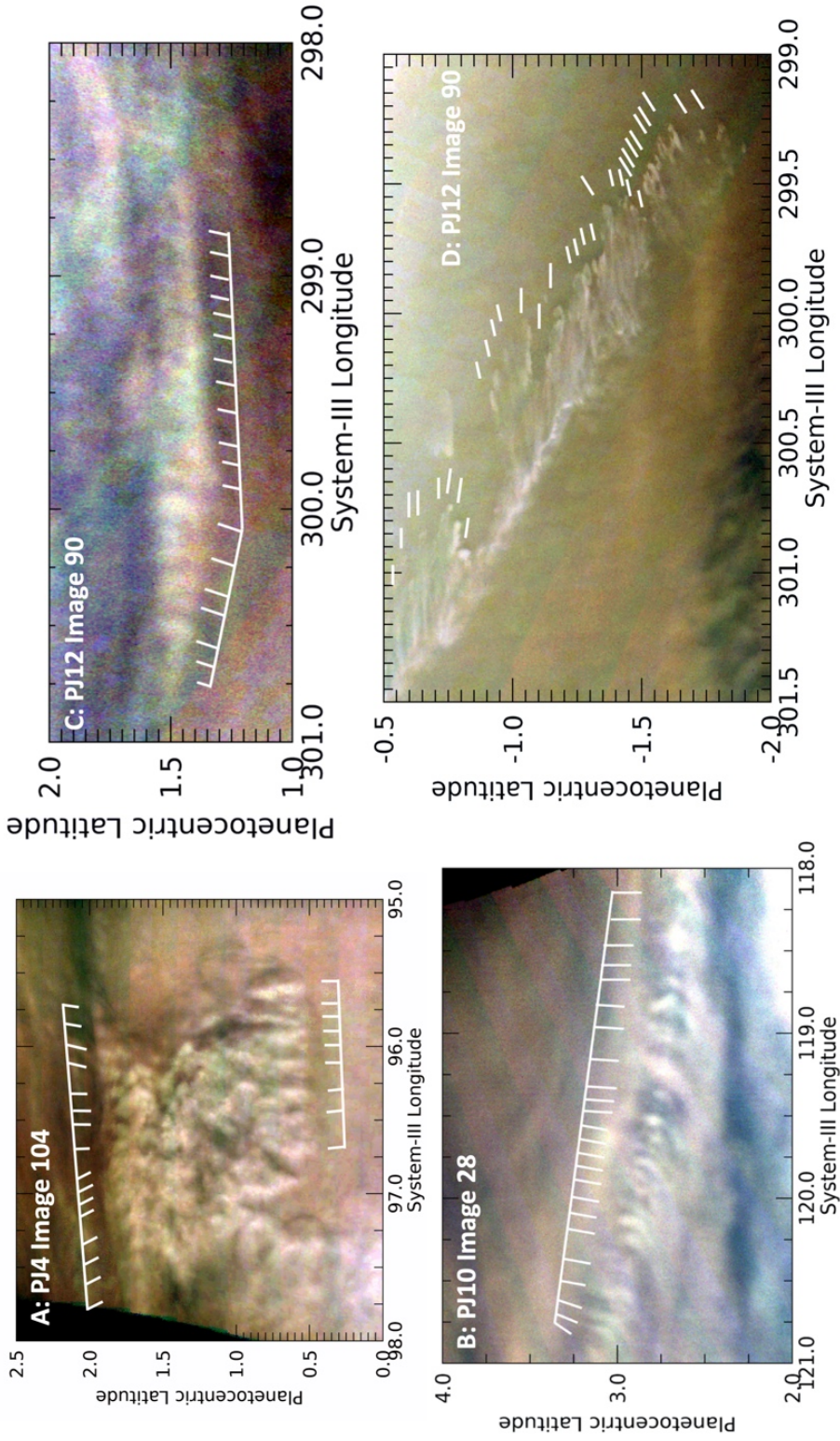
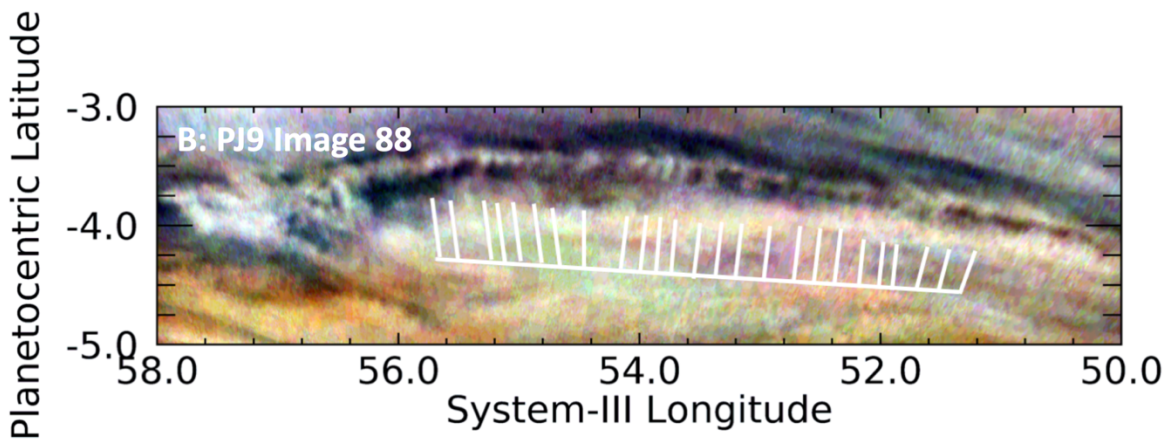
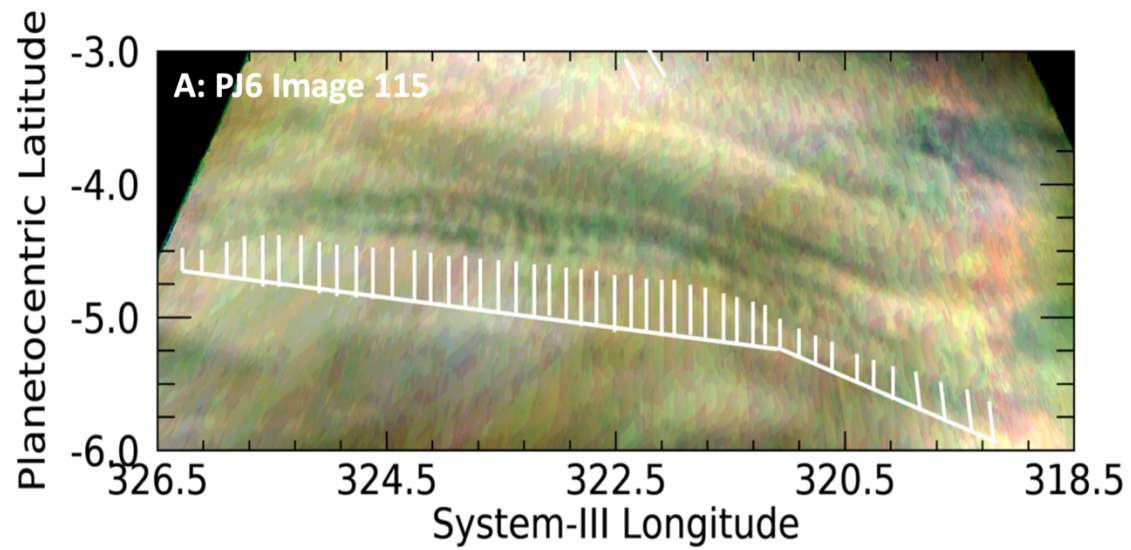


Figure 9. Examples of wave packets defined by bright clouds, all in the Equatorial Zone. Panel A shows a wave packet whose length is roughly equal to its width. Its constituent clouds are clearly higher than their surroundings, given the strong topographic clues from consistent shadowing on their eastern sides. Panel B shows a line of regular clouds with longer, curved southwestern extensions. Panel C shows a similar wave packet of white clouds with narrow wavefronts and a slight curvature. Panel D shows a very curious type of irregular wave-like feature, extracted from the northeastern portion of Fig. PJ12_90a in the Supplemental Information file. The feature is reminiscent of ocean foam, with side-by-side elongated features that are not uniformly directed and may be higher than the surrounding cloud deck, with a consistent darkening on their eastern sides that might be shadowing.



955
 956 *Figure 10. Two detections of regular patterns of relatively bright clouds apparently associated*
 957 *with a fainter central bright region. Both instances involve curved lines. The wave packet in*
 958 *Panel A is associated with a similar but fainter pattern to its north, whereas the wave packet in*
 959 *Panel B has no such association. Both are in the southern component of the Equatorial Zone.*
 960

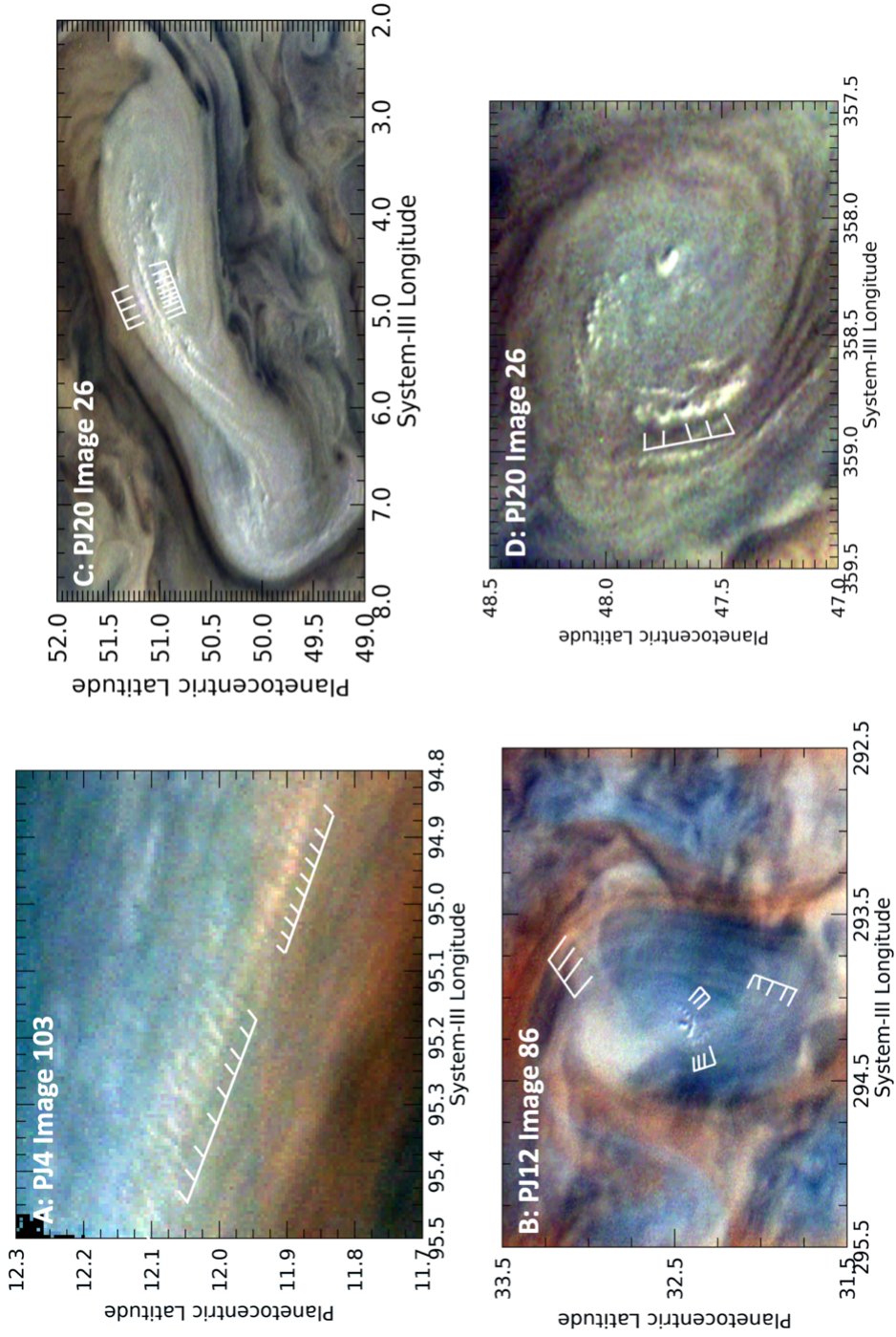
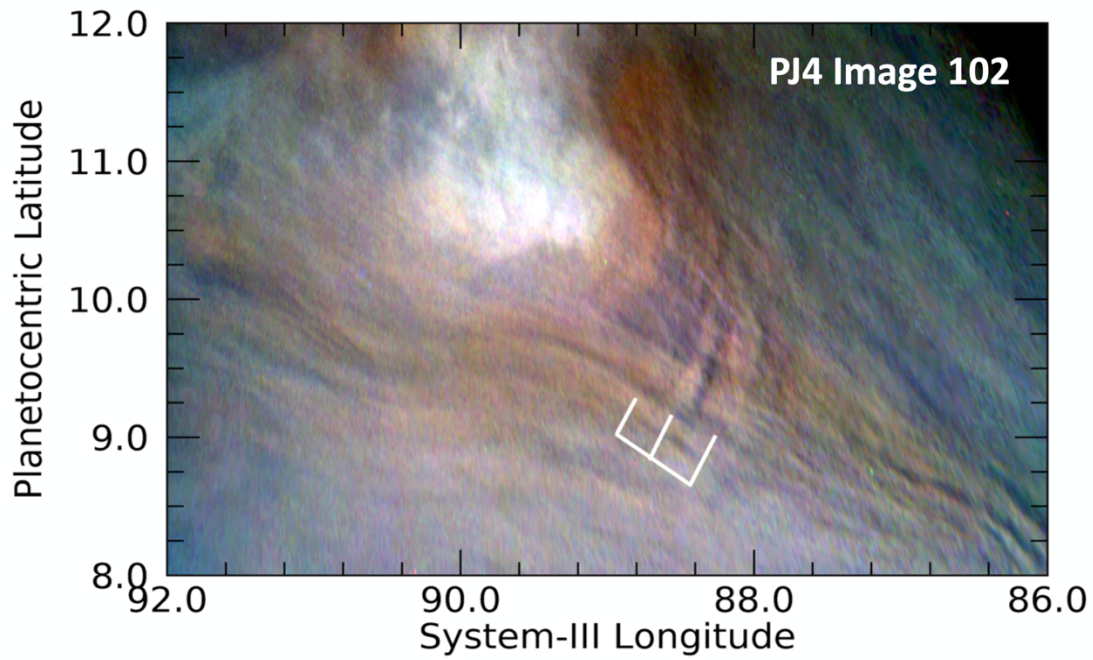


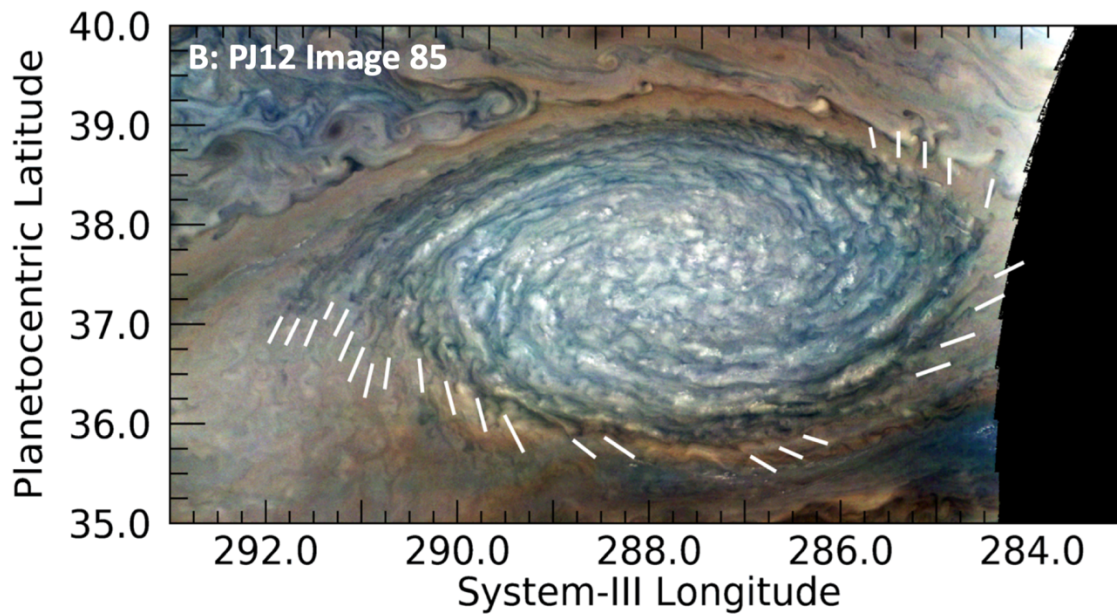
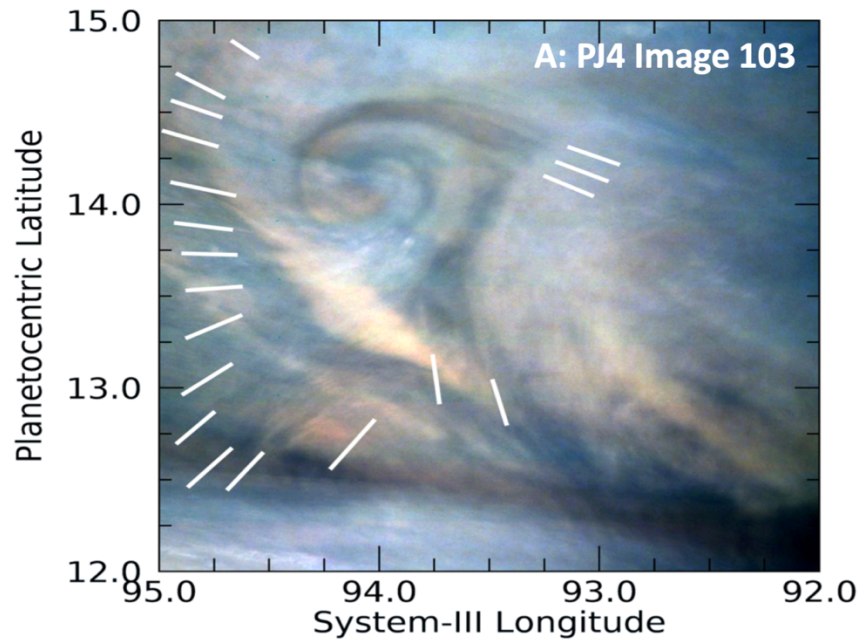
Figure 11. Distinct, very small-scale white clouds with regular spacing. The spacing and the distinct arrangement along a discrete path suggest a wave-like structure. Panel A shows an expanded portion of Fig. PJ04_103b in the Supplemental Information file. Panel B shows a bright cloud, accompanied by short linear arrays of similar bright clouds in an anticyclonic feature in the North North Temperate Belt (NNTB). Panels C and D both show features from the same image in an area just south of the prograde jet at 53°N. From their morphologies, they are both most likely to be anticyclonic vortices.

964



965
966
967
968
969
970

Figure 12. The single unambiguous detection of lee waves in the JunoCam images. We can presume that the long streaks appearing diagonally in this figure are tracking the streamlines of local winds. The lee waves indicated by the white grid lines are orthogonal to the elongated streaks and are likely to be downwind of the bright convective plume in the upper part of this image.



971
 972
 973
 974
 975
 976
 977

Figure 13. Wave-like features detected near vortices. Panel A shows a very compact cyclonic feature with a set of extended radial wavefronts in the North Equatorial Belt (NEB). Panel B shows a regular set of dark lines emerging from the ends of the internal spiral structures in an anticyclonic white oval.

978
979
980
981

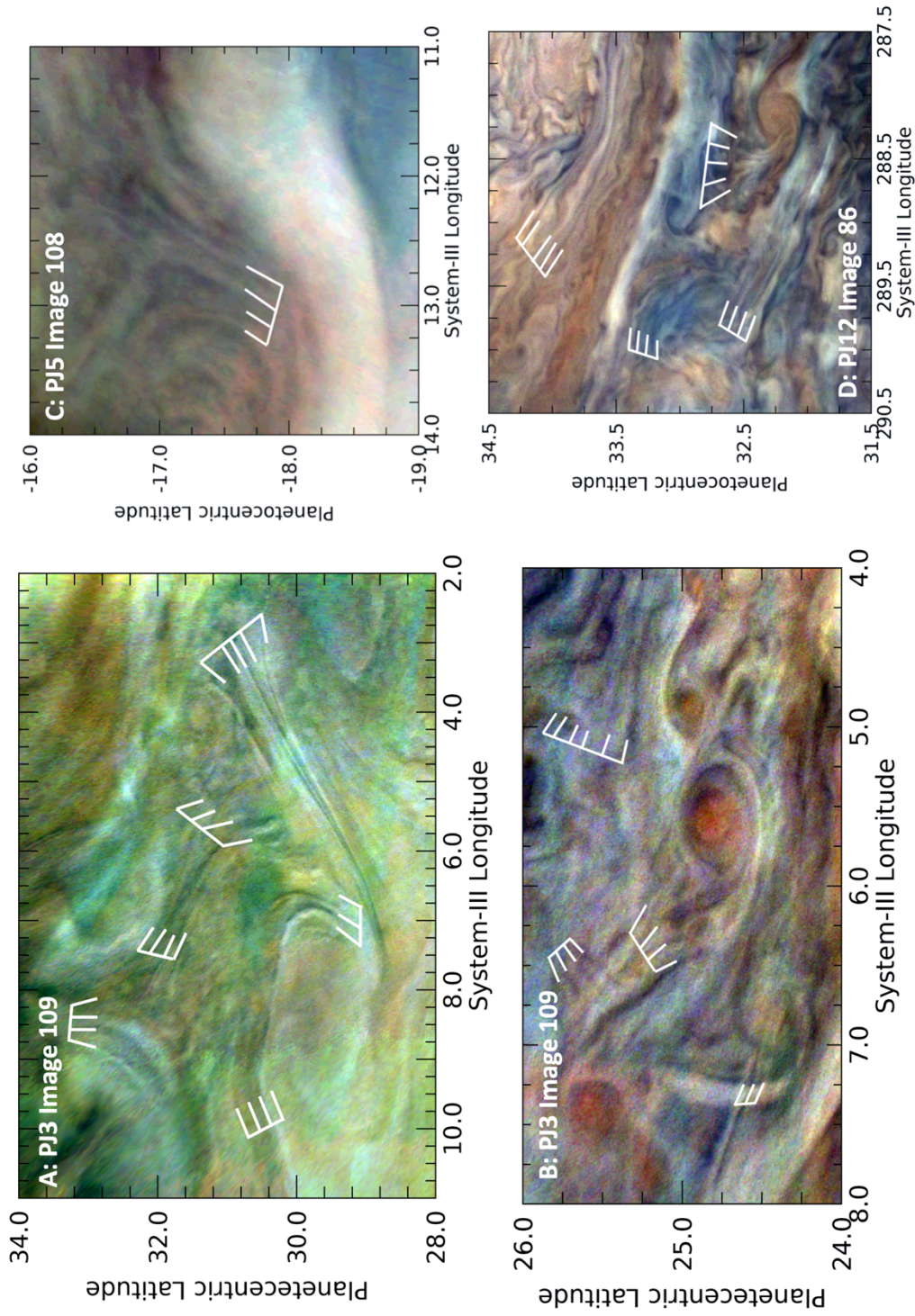
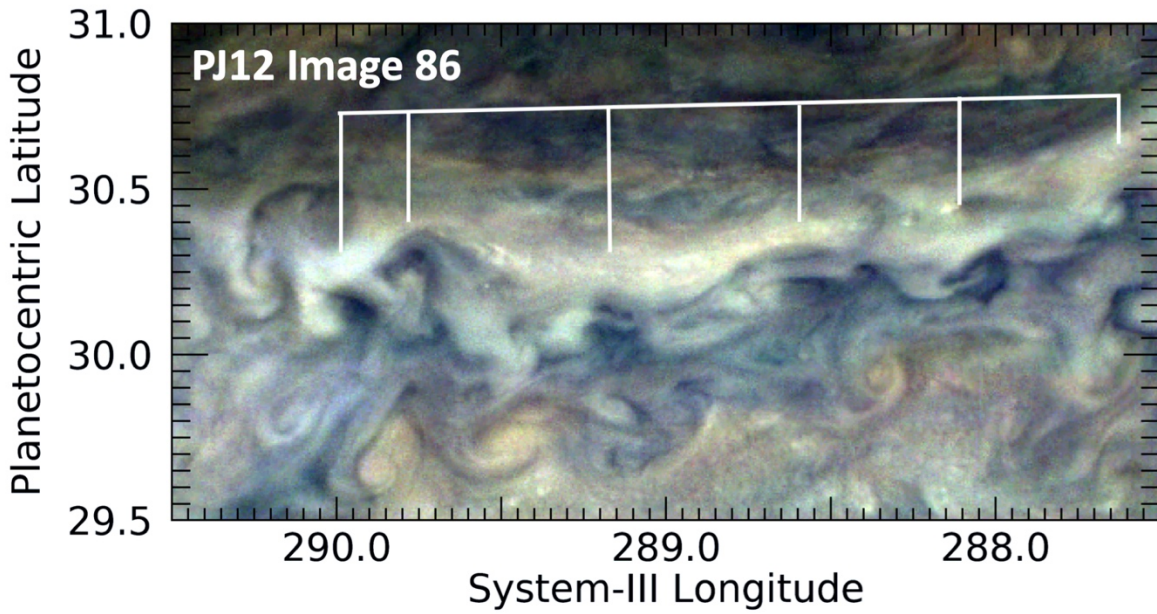
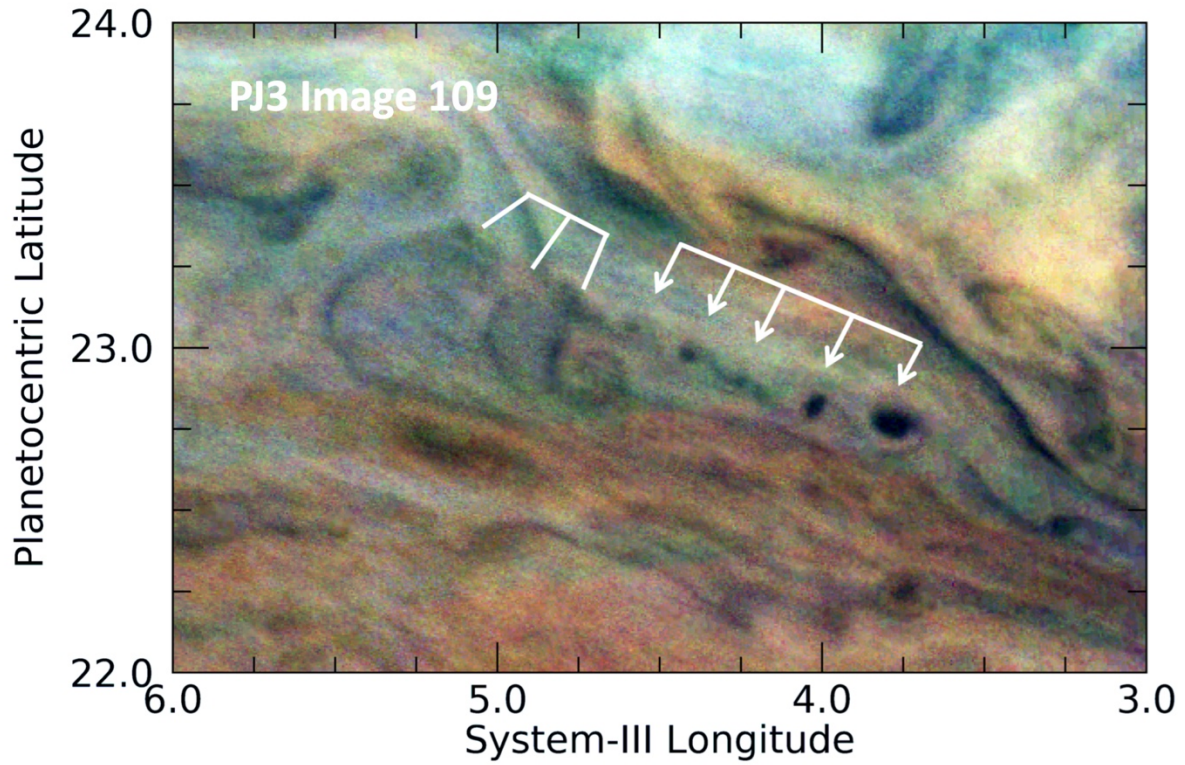
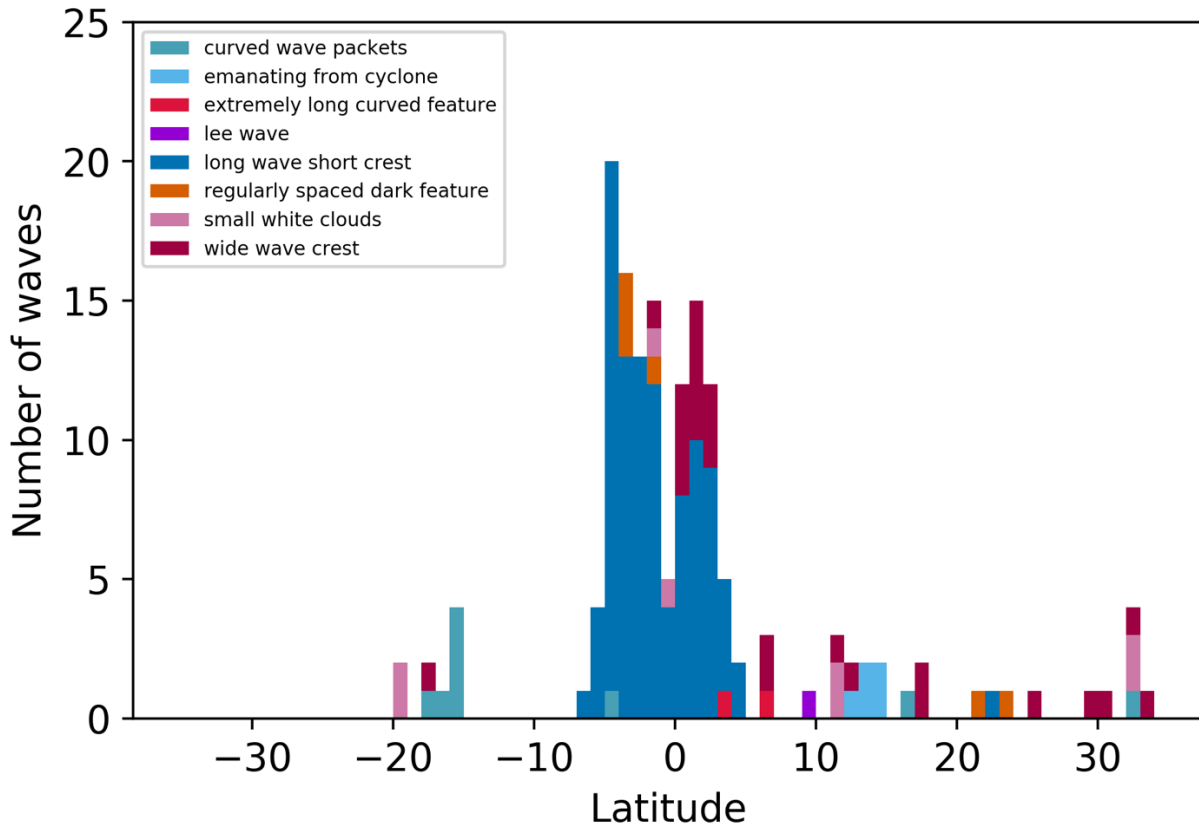


Figure 14. Examples of very long and nearly evenly spaced parallel streaks. Panel A shows several of these detected in a limited region of the North Temperate Zone (NTZ). Panel B shows a region just south of the area in Panel A on the same perijove in the northern component of the North Temperate Belt (NTBn). Panel C shows parallel streaks located in a pale strip of the southern component of the South Equatorial Belt (SEBs). Panel D shows multiple examples of parallel cloud streaks in the North North Temperate Belt (NNTB).

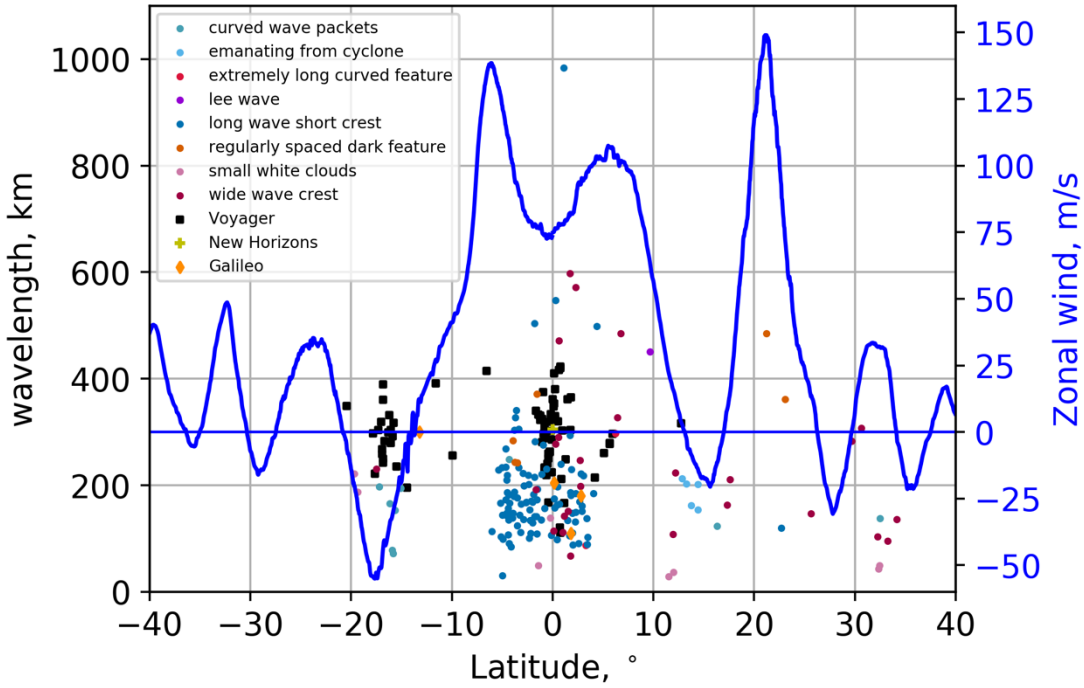


983
 984 *Figure 15. Unusual quasi-wave-like features in the northern hemisphere. Panel A illustrates three*
 985 *curved wavefronts next to relatively dark circular features indicated by the arrows. Panel B shows*
 986 *a series of repeated patterns in the North Temperate Zone.*

987
 988
 989
 990
 991



993
 994 *Figure 16. Histogram of waves and wave-like features detected in PJI-20 by JunoCam. Different*
 995 *types of waves and wave-like features are denoted by different colors and identified by the key.*
 996 *Each corresponds to a different wave morphology as discussed in Section 3.2. The bin size is 1°*
 997 *in latitude.*
 998



999
 1000
 1001
 1002
 1003
 1004
 1005
 1006
 1007
 1008

Figure 17. Wavelengths of waves and wave-like features detected in PJ1, PJ3-PJ20 by JunoCam. Measurements of different types of wave morphologies are color-coded as in Figure 15. Mean zonal wind velocities for 2017-2018 (Wong et al. 2020) are plotted in blue. Values for Voyager, New Horizons and Galileo are taken from their respective references in Table 1. Wavelengths for wave packets detected by HST and ground-based images (Simon et al. 2018, Fletcher et al. 2018) are greater than 1100 m/s and clustered around 14.5°N (see Table 1).